UNIVERSITY OF COPENHAGEN
FACULTY OF SCIENCE

NIELS BOHR INSTITUTE

Structural Characterization of Superconductor-Semiconductor Hybrid Crystals

Master's thesis

Martín Espiñeira Cachaza

Supervirsors: Peter Krogstrup
Jesper Nygård

September 2018

ABSTRACT

Hybrid III-V semiconductor-supeconductor nanowires are candidates to become qubits in a universal quantum computer, performing braiding operations of Majorana zero modes. Vapour-Liquid-Solid and Selective Area Growth nanowires are the two most used techniques to grow these NWs. With the increasing interest on fabricating these structures comes the necessity to understand the hybrid structure formed in the interface between the superconductor and the semiconductor. This thesis focus on the study of the structure of this hybrid interface in both VLS and SAG nanowires. VLS nanowires showed a perfect epitaxy between the InAs and Al at the interface with the development of twin grains in the Al. As well it is presented the Geometric Phase Analysis technique to study crystal strain in SAG nanowires. This technique shows the dilatation and rotation of a selected set of planes along the transition between the buffer and the NW, as well as the appearance of misfit dislocations in the interface. The Al deposition was found to be monocrystalline along the SAG nanowire facet.

ACKNOWLEDGMENTS

First of all I want to thanks Peter Krogstrup for giving me the opportunity of joining his group and for his guidance and help. I can't image a better way for me to start in the research field than belonging for 1 year to this world class department and research group. There are not enough pages to write how many things I learned this year, and not only related with science but with life in general.

I feel deeply grateful to all the people that taught me, with high doses of patience and repetition, all the experimental techniques that I learned. The first one in this list is Erik Johnson. All the hours spent in the TEM in Risø had a tremendous value to me. I want to say huge thanks as well to Sara Martí and Jordi Arbiol for hosting me in my visit to their institute ICN2 in Barcelona. The data acquired with Sara during those days in the Titan microscope in Zaragoza was extremely useful and a core part of the results in this Master thesis. Thanks to Shivendra, Nader and Thomas Kanne for very useful discussion and training.

My GPA code would have never existed without the incredible help and supervision of Tomaš Stankevič. It is always easier to tell the result instead teaching why something does not work, and you always chose the second option.

I feel very lucky as well for the atmosphere created in the office this last winter with all the colleagues. Joachim was my in-game supporter when I really needed a brake and that was highly valuable for me.

Last and most important, I want to thank all the people that morally supported me in these two years. María for infinite support all the time, my family for making my dreams come true and my friends from Madrid for receiving me always as if I had never left. Although being 2.000 km apart from all of you I always felt very close to you. Gracias a todos.

MARTÍN ESPIÑEIRA CACHAZA
Copenhagen
September 2018

Contents

List of Figures

Motivation and Introduction 1

Quantum information

In the decade of the 50's Gordon Moore proposed a trend, *Moore's law*, about the evolution of integrated circuits suggesting that the number of transistors in computers will double up every two years[1]. This trend started to get to its end in the early 90's where the community began to realize that fundamental thermodynamical limits where being reached in the development of new transistor generations[2].

In the last two decades there has been an increasing interest in developing universal quantum computers that take advantages of quantum mechanics, such as superposition and entanglement, in order to increase their computing power. Such machines would provide fast solutions to computational problems that need an increasing exponential time to be solved by ordinary computers, such as discrete logarithms and factoring problems[3;4;5]. In order for these machines to work they have to fulfill the so called *Di Vicenzo criteria* which describes the basic requirements for the physical realization of quantum computation[6].

Nowadays there are many approximations to generate qubits , the essential block of the universal quantum computer. The five most relevant ways to generate these experimental setups require are: impurity spins[7;8], trapped ions[9;10], superconducting circuits (or transmon devices)[11;12], linear optics[13] and topologically protected semiconductors[14;15]

The first proposal for the realization of a topological protected qubit was in 2003[16] and since then this type of qubit approximation has attracted a lot of interest. It was proposed that a system formed by anyons and their excitations (which obey non-abelian statistics) can be considered as a quantum computer with the advantage that it would be fault-tolerant, unlike the other qubit prototypes[17].

Years later, it was demonstrated that the behaviour of electrons under some exotic conditions creates a quasiparticle that behave like a non-abelian anyon, called Majorana fermion[18]. Moreover, these Majorana fermions would appear in semiconductor-superconductor heterostructure[19] like a III-V semiconductor nanowire (NW) with a superconducting metal deposition on it[20]. Some studies have been done as well on optimization of NW design and arquitechture to create a topological universal quantum computer[21;22].

A NW is a crystalline object with cilindric or elongated shape and dimensions of ~ 100 nm in the radial dimension and few μm in the longitudinal direction, a quasi-1D object. Unlike the bulk materials, it is this constrain in the radial dimension what makes them to show quantum behaviours under certain conditions[23]. III-V nanowire heterostructures, that are of interest in this Master Thesis, are grown with the Molecular Beam Epitaxy (MBE) technique by two different growth mechanisms: Vapour-Liquid-Solid (VLS)[20;24;25] and Selective Area Growth (SAG)[26;27;28].

A MBE system typically consists in a series of different chambers where the substrate on which the growth is going to occur can be inserted, manipulated, grown and analysed[29;30;31] all under Ultra High Vacuum (UHV conditions). In Fig. 1.1 there is an schematic description of the growth chamber where the crystal is built up. Although the figure shows the basics of what it is inside a growth chamber it can be added as well other instruments to monitor the growth of individual layers of crystal like Reflection High-Energy Electron Diffraction (RHEED)[32] or the adaptation of Transmission Electron Microscopes (TEM) to observe even in a more precise way in real time the growth of the crystal[33]

All this facts made the research of III-V semiconductors NWs fabrication an even more interesting field with great capabilities and potential, specially in the

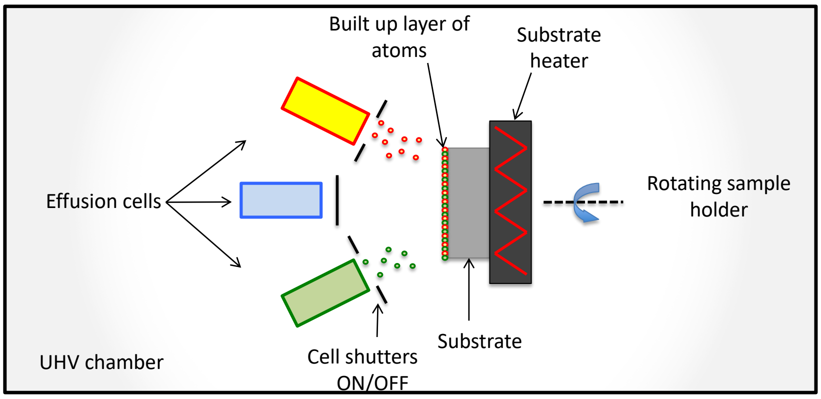

FIGURE 1.1: Basic schematics of the growth chamber from a MBE system. Its extremely controlled conditions, cleanliness and UHV allows to grow crystalline structures in a precise way. The effusion cells are heated up to hundreds of degrees °C to expell an accurate beam of atoms or molecules and deposited on top of the substrate to create a highly uniform crystal. Each cell contains a different substance and can be opened and closed with a cell shutter. The substrate has to be heated up as well and rotating while the growing process to homogenize the growth of the crystal.

realization of a future fault-tolerant qubit. Inherently with this fact, it comes as well the importance of characterizing the cristalline structure, semiconductor electrical properties and chemical composition of the prototypes that are being grown nowadays[28;34]. Characterization is an essential part in this field since it confirms growth hypothesis, corroborates how good a sample is and guides the research towards the next step.

Thesis Outline

This thesis covers the characterization of different samples of III-V nanowires, grown by the methods Vapour Liquid Solid (VLS) and Selective Area Growth (SAG), by Transmission Electron Microscopy (TEM) and the use of Geometric Phase Analysis (GPA) method to study the strain induced in the interfaces of the different crystals that form a SAG nanowire. This information was used as feedback to the different people that are involve in the growth part of the group, to understand and to interpret the result of different NW growths as well as the optimization of the growing process.

In this document appear several TEM images which are inherently in black and white and sometimes with detailed gray contrast. Printed versions risk having poor quality in this images depending on the printer so it is recommended to see the images in the PDF version.

The TEM images taken in this thesis come from 3 different microscopes:

1. A FEI-Philips CM20 TEM[35] located in the HCØ building from the University of Copenhagen.
2. A JEOL JEM 3000F[36] located in the Denmark Technical University Wind Energy Department at Risø.
3. A FEI Titan STEM[37] located in the LMA lab from University of Zaragoza (Spain).

Theory on III-V/FCC crystals and GPA 2

This chapter covers the main theoretical aspects on this work. The first part establish the main crystallographic structures and properties of type III-V NWs. Unlike bulk materials, these NWs can show two different crystalline structures[38]: *wurtzite* as a hexagonal structure that does not appear in bulk III-V semiconductors and *zincblende*. The stacking sequence and the most common crystallographic defects form these structures are explained.

The second part is the mathematical and physical description of the Geometric Phase Analysis (GPA) method. This method is used to study lattice strain inside crystals in High Resolution Transmission Electron Microscopy (HR-TEM) images[39] by analyzing the phase component of the Fourier transform of a crystal, which includes information about the position of every atom in the image. Images from SAG NWs cross sectional cuts are an ideal example to use on this method since the lattice mismatch between the NW and buffer induces a strain in the NW compared to the unstrained bulky substrate. This experiments will be shown in Chapter 4.

2.1 Crystallography

WZ and ZB structures

Type III-V semiconductors have two main crystal structures: zincblende (ZB) and wurtzite (WZ). In bulk material only ZB is a stable phase for III-V, except for some kind of III nitrides elements where it is stable[40;41]. In NWs both ZB and WZ and mixtures are possible.

The unit cell of ZB structure consists in group V atoms sitting in the corners and the center of the faces of a cube, each connected with four group III atoms forming a tetrahedron. Fig. 2.1 a) is a model of a III-V ZB unit cell. All sides of the unit cell have equal length. The growth direction of ZB NWs is the [111]. The repetitively ordered placement of unit cells to form the crystal is called stacking sequence and in the case of ZB it is repeated every 3 bilayers of crystal, denoted as 3C in Ramsdell notation. A bilayer is defined as a one layer if V atoms and one layer of III atoms that makes a primitive cell. The stacking sequence for ZB is described as ABCABC as illustrated in Fig. 2.1 b) where symmetric layers have the same color.

The unit cell of WZ structure consists in III atoms sitting in the corners of a rhombic figure with angles of 60° and 120° and V atoms in a tetrahedral position around the III atoms. Fig. 2.1 c) is a simulation of a WZ unit cell. The arrangement of these rhombic unit cells create an hexagonal compact structure. The stacking sequence for WZ has a two bilayer periodicity in the form ABAB as seen in Fig. 2.1 d), also called 2H in Ramsdell notation. The growth direction in WZ NWs is [0001], in hexagonal coordinates.

Other more complicated crystal structures can appear with less probability in III-V NWs, such as the hexagonal 4H structure with a stacking sequence ABACABAC.

Stacking faults and other structures

A stacking fault is a crystal planar defect created when a different layer is added to the stacking sequence. In a WZ structure the addition of a C plane in the form ABAB C ABAB would create a stacking fault. Fig.4.3 b) from Chapter 4 is a

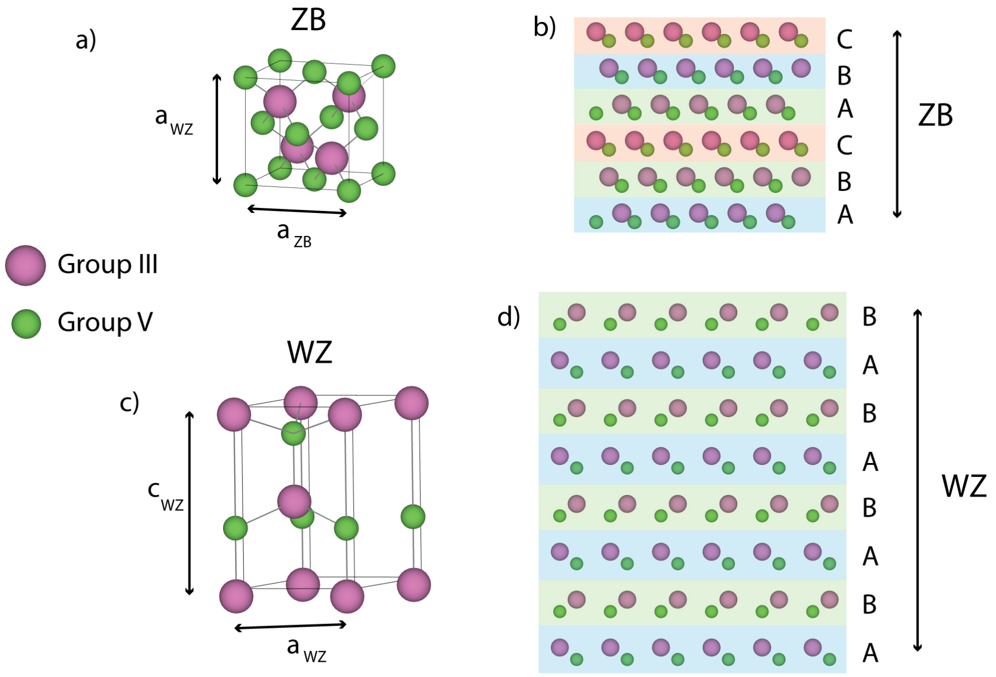

FIGURE 2.1: ZB and WZ structures in III-V crystals. **a**) ZB unit cell. **b**) ZB stacking sequence. **c**)WZ unit cell. **d**) WZ stacking sequence.

stacking fault in the stacking sequence of a WZ InAs NW.

FCC

FCC metals are useful to create hybrid III-V semiconductor-superconductor hybrid crystals. Fig. 2.2 a) is a simulation of a FCC unit cell crystal. The two most common epitaxial growth directions between a III-V NW and a FCC metal are described in Fig. 2.2 b) and c).

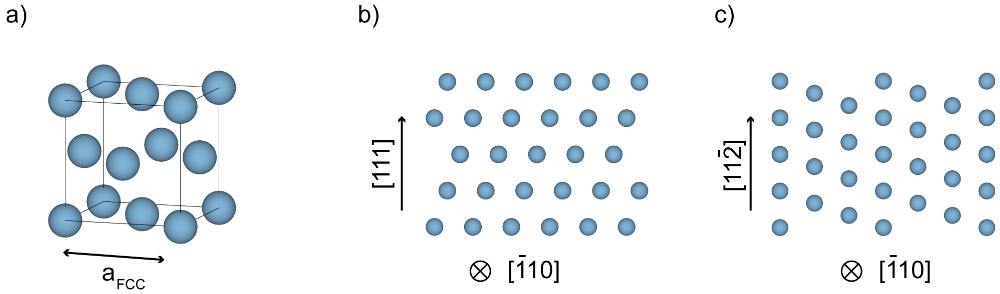

FIGURE 2.2: FCC structure in metals. **a**) FCC unit cell. **b**) FCC [111] upwards direction and [$\bar{1}$10] out of plane orientation. **c**)FCC [11$\bar{2}$] upwards direction and [$\bar{1}$10] out of plane orientation.

2.2 Geometric Phase Analysis

Geometric Phase Analysis (GPA) is a method for mapping strain fields and individual atom displacement from crystals in High Resolution TEM (mode explained in Chapter chapter 3) images[39;42]. This method, unlike CBED (explained in Chapter chapter 3), allow to measure strain in regions with a high strain gradient[43]. By combining GPA with electron tomography it can be obtained as well a 3D strain map of a sample[44].

The main idea behind GPA is to mask a Bragg peak in the power spectrum of the Fourier transform of a HRTEM image and performing the inverse Fourier transform. The phase of this complex image (it has real and imaginary part) contains information about the displacement of atomic planes. The strain filed is then extracted from the displacement.

2.2.1 Fourier description of a set of planes

A HRTEM image with multiple crystal periodic planes can be defined as a Fourier series as follows:

$$I(\boldsymbol{r}) = \sum_{g} H_g \exp(2\pi \boldsymbol{g} \cdot \boldsymbol{r}) \tag{2.1}$$

where $I(\boldsymbol{r})$ is the image intensity at a position $\boldsymbol{r}$, $\boldsymbol{g}$ is a vector in the reciprocal space defining a set of lattice planes and H_g are the Fourier coefficients:

$$H_g = A_g \exp(iP_g) \tag{2.2}$$

with A_g the amplitude in the power spectrum of the planes defined by $\boldsymbol{g}$ and P_g the phase. Merging together eq. 2.1 and eq. 2.2:

$$I(\boldsymbol{r}) = A_0 + \sum_g 2A_g \cos(2\pi \boldsymbol{g} \cdot \boldsymbol{r} + P_g) \tag{2.3}$$

which is the general general description of a perfect crystal as a Fourier series. A selected set of planes defined by $\boldsymbol{g}$ is described as:

$$B_g(\boldsymbol{r}) = 2A_g \cos(2\pi \boldsymbol{g} \cdot \boldsymbol{r} + P_g) \tag{2.4}$$

At this point a desired $\boldsymbol{g}$ is selected in order to study the displacement of the atoms that belong to that periodicity. We will consider this $\boldsymbol{g}$ as a reference region with no strain.

2.2.2 Change in periodicity implies displacement

Now we consider that a selected $\boldsymbol{g}$ differs from a reference region either because it is a strained region, there is a chemical change or other reason. This means:

$$\boldsymbol{g} \rightarrow \boldsymbol{g} + \Delta \boldsymbol{g} \tag{2.5}$$

So rewriting eq. 2.4 with this new condition:

$$B_g(\boldsymbol{r}) = 2A_g \cos(2\pi \boldsymbol{g} \cdot \boldsymbol{r} + 2\pi \Delta \boldsymbol{g} \cdot \boldsymbol{r} + P_g) \tag{2.6}$$

where P_g is a phase constant set to 0. Comparing eq. 2.6 and eq. 2.4 we obtain an expression which correlates the phase of the original image with changes in the reciprocal space vector $\boldsymbol{g}$:

$$P_g(\boldsymbol{r}) = 2\pi \Delta \boldsymbol{g} \cdot \boldsymbol{r} \tag{2.7}$$

Taking the gradient into eq. 2.7 we get:

$$\nabla P_g(\boldsymbol{r}) = 2\pi\Delta\boldsymbol{g} \tag{2.8}$$

which is an equation that indicates that differences in $\boldsymbol{g}$ are equal to differences in image's phase slope. Eq. 2.8 establish the main idea behind the GPA method. An strained region from an image will have an slight $\Delta\boldsymbol{g}$, compared with the $\boldsymbol{g}$ from a relaxed region, which can be detected as differences in the phase of the image.

As a matter of simplicity eq. 2.7 can be rewrite as a function of displacement with the variable change $\boldsymbol{r} \to \boldsymbol{r} - \boldsymbol{u}$ where $\boldsymbol{u}$ is the displacement field:

$$P_g(\boldsymbol{r}) = -2\pi\boldsymbol{g} \cdot \boldsymbol{u} \tag{2.9}$$

As eq. 2.9 $P_g(\boldsymbol{r})$ gives the displacement in the same direction as the selected $\boldsymbol{g}$ vector, it is convenient to get the full displacement map from the original image. This is done by selecting another set of planes, a $\boldsymbol{g}$ non colinear with the first one, and repeating the same procedure as done before. Solving the system of 2 equations and isolating the displacement we get the relation

$$\boldsymbol{u}(\boldsymbol{r}) = -\frac{1}{2\pi}\left[P_{g1}(\boldsymbol{r})\boldsymbol{a}_1 + P_{g2}(\boldsymbol{r})\boldsymbol{a}_2\right] \tag{2.10}$$

where $\boldsymbol{a}_1$ and $\boldsymbol{a}_2$ are vectors in the real space in the same direction as $\boldsymbol{g}_1$ and $\boldsymbol{g}_2$ in the reciprocal space. Eq. 2.10 is the full displacement of the image.

2.2.3 Strain tensor

The strain e is defined as the derivative of the displacement $\boldsymbol{u}$. The derivate of eq. 2.10 has four components since it is a vector and can be written in matrice notation as:

$$e = \begin{pmatrix} e_{xx} & e_{xy} \\ e_{yx} & e_{yy} \end{pmatrix} = \begin{pmatrix} \frac{\partial u_x}{\partial x} & \frac{\partial u_x}{\partial y} \\ \frac{\partial u_y}{\partial x} & \frac{\partial u_y}{\partial y} \end{pmatrix} = -\frac{1}{2\pi}\begin{pmatrix} a_{1x} & a_{2x} \\ a_{1y} & a_{2y} \end{pmatrix}\begin{pmatrix} \frac{\partial P_{g1}}{\partial x} & \frac{\partial P_{g1}}{\partial y} \\ \frac{\partial P_{g2}}{\partial x} & \frac{\partial P_{g2}}{\partial y} \end{pmatrix} \tag{2.11}$$

Eq. 2.11 can be decomposed in symmetric and antisymmetric part

$$\varepsilon = \frac{1}{2}(e + e^t) \tag{2.12}$$

$$\omega = \frac{1}{2}(e - e^t) \tag{2.13}$$

where ε is the dilatation part of the strain tensor and ω is the rotational part. Any type of deformation of a crystal can be described as a linear combination of ε and ω.

The power of the GPA method is that by studying the phase of a HR TEM image we can obtain valuable information such as the two different types of deformations that can happen in a crystal, dilatation and rotation.

2.2.4 Test crystal

In order to test the MatLab code it will be applied to an image from a structure generated by computer. This crystal has controlled interface parameters between two regions so it can be used as a calibration for the program.

For simplicity the crystal was simulated in 1D with only periodicity in the vertical axis, as appears in Fig.2.3 a). The crystal has three phases: left, middle and right. The left part is equal to the right and they have a lattice spacing of 15 pixels and the middle part have a lattice spacing of 14 pixels. A program was used to apply a blurring effect to each pixel in order to add more realism in the FFT power spectrum.

In fig. 2.3 are the main steps needed to perform a GPA analysis to an image. Fig. 2.3a) is the simulated crystal used in this test. The relative strain, or compression, between the lateral and the central part is 7.14%. A Hann mask was used in the image before performing the Fast Fourier Transform (FFT) in order to avoid streaking effects in the power spectrum. b) Is the FFT from a). The central peak is removed since the mean value of the image was subtracted in a) for simplicity. Although the peak appears to be a single peak it contains the crystal information from the vertical planes from the lateral and central regions.

Fig. 2.3 c) illustrates the desired set of planes that we want to study, by using a gaussian mask in the Brag peak. In this case it is obvious that we want a vertical

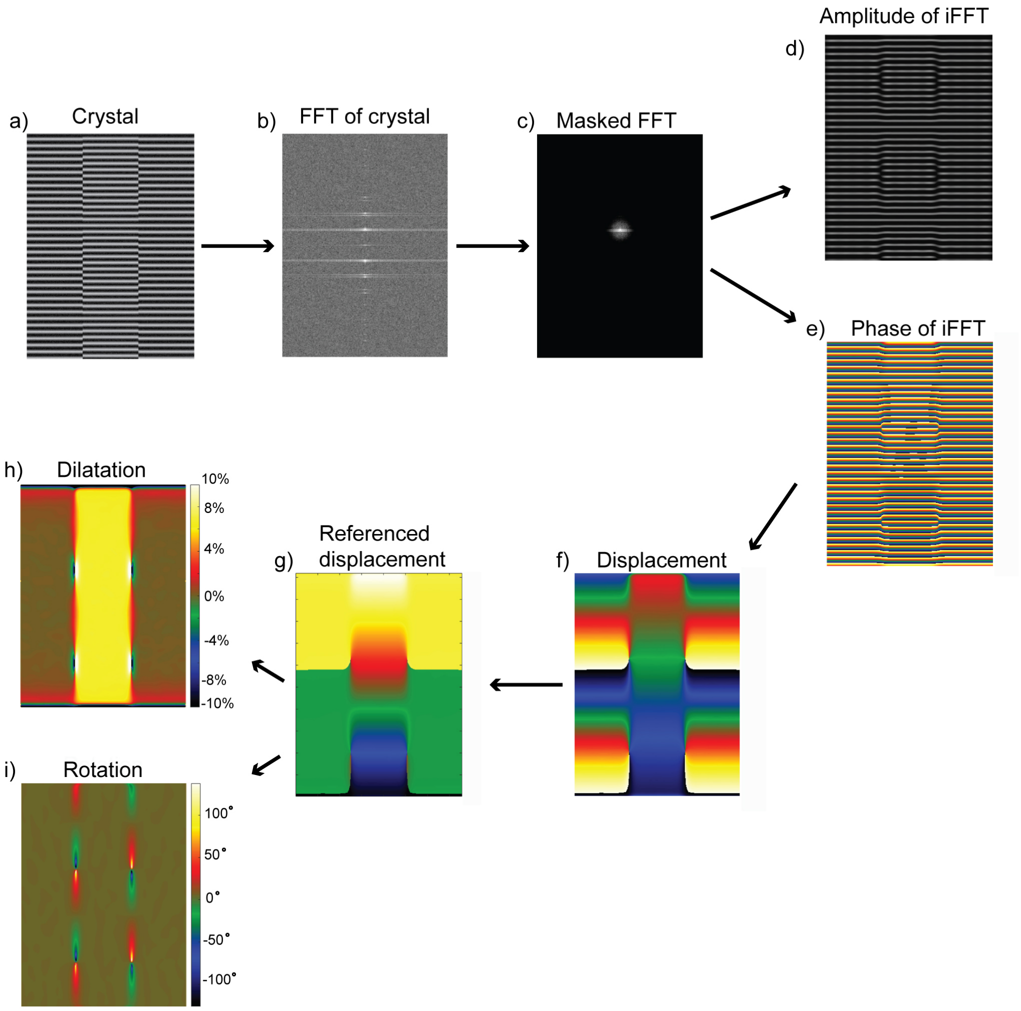

Figure 2.3: GPA process described in steps with a sample crystal. **a**) Image of the sample crysta;l. **b**) FFT power spectrum of the crystal. **c**) Gaussian mask applied to the desire peak in b). **d**) Amplitude part of the iFFT. **e**) Phase part of the iFFT. **f**)Displacement obtained using eq. 2.9. **g**) Displacement after setting the left part as 0 strain region. **h**) Dilatation map of the crystal with the expected 7% dilatation value in the center part. **i**)Rotation map of the crystal.

peak since it is where it is contained all the information of the image. d) And e) are the amplitude and phase of the inverse FFT from the masked peak in c). The phase have a lot of sharp transitions because MatLab automatically wraps it. This means that the phase values only go from -π to π values. An unwrapping code was used for better visualization but discarded for the high cost of time in the process (>60 s per image). The final result is not affected by working with a wrapped phase.

In fig. 2.3f) is the displacement obtained with the 1D equation derived in the previous section, eq. 2.9. Image g) shows the displacement after subtracting the chosen reference region to be unstrained. In this case the reference region was the left part of the crystal. The sharp transition from yellow to green in the lateral parts comes from the fact of working with a wrapped phase. Nevertheless this does not affect the result. h) Is the dilatation map from the sample. It can be checked that the expected 7% compression value is obtained. i) is the rotation map of the vertical planes, which shows 0° as this is basically a 1D system. The high strain and rotation spots from h) and i) come from the fact that the crystal rows do not match in that exact point and the program interprets it as a discontinuity in the crystal, leading to an enormous dilatation and rotation. A real crystal example will be shown in Fig. 4.10 where misfit dislocations behave in a similar way concentrating a lot of strain.

Experimental techniques 3

This chapter will explain the main techniques used for the realization of this work. The most used set up were different models of Transmission Electron Microscope (TEM) which were used in different observation modes to characterize nanowires of the type VLS and SAG. Apart from this, other set ups were used for the required sample preparation and management.

3.1 TEM

TEM is one of the most used tools to characterize the structure and composition of samples in the nm range from different areas in science like physics, chemistry or biology. The idea is to study 3D samples like crystals or biological specimens and make a magnified image that will be a 2D projection of them.

The main purpose behind TEM microscopy is to illuminate with a uniform electron beam a sample with a thickness of hundreds of nm. The sample has to be thin enough to allow the electrons pass through, which in case of nanowires (NWs) is not a problem as they have diameters of ∼100 nm. The electrons are generated by an electron gun with a constant electron current density, accelerated to a range of energies around 80 - 300 keV and focused into the specimen by a set of two or three lenses called *condenser lenses system*. Then all electrons transmitted through the specimen (both non-diffracted and diffracted) are collected by a set of lenses called *objective lenses* and *intermediate lenses* which form the image in the desired observation mode through the placement of apertures and choosing the focal distance. In the end, the image is formed and magnified again by a set of lenses called projector lenses which project the image into a fluorescent screen or a CCD camera. In Fig. 3.1 a) appears a schematic model of a TEM with the basic components needed to form it. In b) it is marked with red arrows the approximate position of each component in a JEOL 3000F TEM used during this thesis.

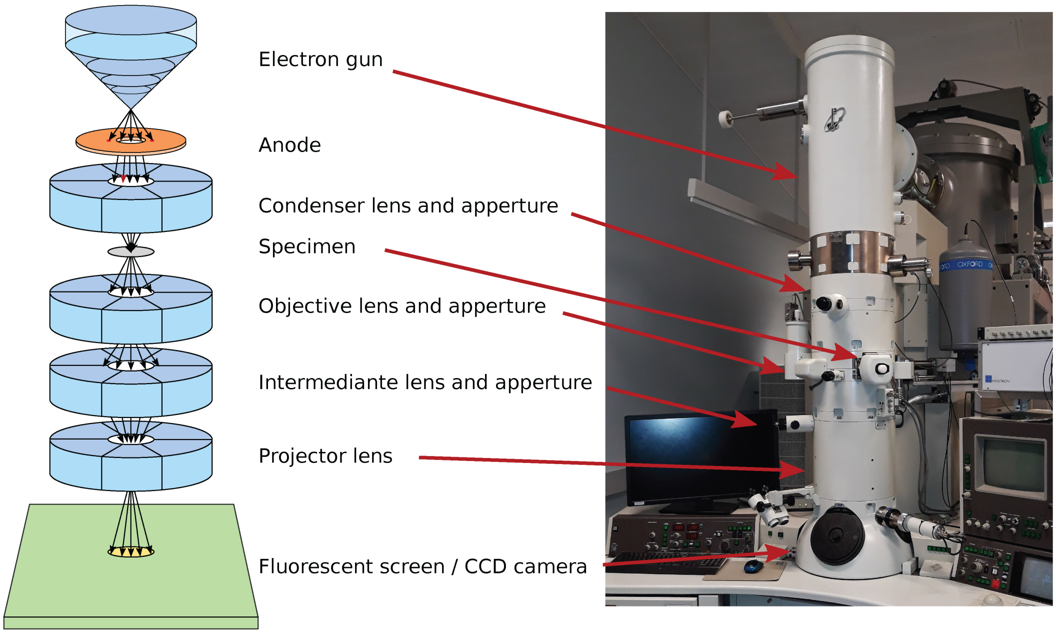

Figure 3.1: Schematics of a TEM and comparison with a JEOL JEM 3000F used during this master thesis

The main advantage of TEM microscopy compared to other systems like Scanning Electron Microscopy (SEM) is the wavelength associated to the electrons that illuminate the sample. Since electrons are typically accelerated to 200-300 keV it is necessary to use the relativistic corrections from in eq. 3.1

$$\lambda_e \approx \frac{h}{\sqrt{2m_e E\left(1+\frac{E}{2m_0c^2}\right)}} \tag{3.1}$$

where λ_e is the wavelength of the electrons, m_e is the mass of the electron and E is the energy. For the FEI-Philips CM20 TEM used, which has an acceleration voltage 200 kV (and thus accelerates electrons to energies of 200 keV) the associated wavelength is 0.025 Å. This result can only be used as a theoretical limit of the resolution when using this electrons since in reality no microscope have such a small resolution. The real resolution is strongly affected by aberrations generated by the lenses, stability of the microscope and many other factors. Nowadays the best TEMs have a resolution up to ~0.5 Å.

There are different modes of TEM depending on the microscope set up and which information we want to get from the sample. Some of these modes are: Conventional Transmission Electron Microscopy (CTEM), High Resolution Electron Microscopy (HRTEM), Scanning Transmission Electron Microscopy (STEM), Electron Tomography (ET), Electron Energy Loss Spectroscopy (EELS) or Energy Dispersive X-ray spectroscopy (EDX) among others.

In the coming sections it will be described the main parts that form a TEM and the most used observation modes. Although almost all the electrons that form an image in a TEM travel through the sample, an thus they are transmitted, as notation it will be used the term *transmitted* electrons only for electrons that did not suffer any scattering in diffraction by planes.

3.1.1 Observation modes

For better understanding in the next figures it will be shown a simplified model of a TEM eliminating all the parts that are not essential for explaining the differences between the observation modes. For this reason, condenser and projector lenses are eliminated since they are not relevant to explain the different TEM modes.

It will be assumed that the specimen is illuminated with monochromatic and parallel beam o electrons and that the lenses are perfect, meaning that they do not have any of the common aberrations that the have in the real world such as chromatic, spherical or coma. As well we consider that all the electrons travel parallel to the optical axis. The angle of the diffracted electron rays is highly exaggerated in the figures in order the make easier the distinction form the transmitted ones. In reality diffracted electrons have solid angles in the order of ∼ mrad.

Image mode or conventional TEM

The simplest way to observe a sample in the TEM is using image mode or Conventional TEM (CTEM). Fig. 3.2 describes a ray diagram of a simplified TEM describing how the magnified image is made.

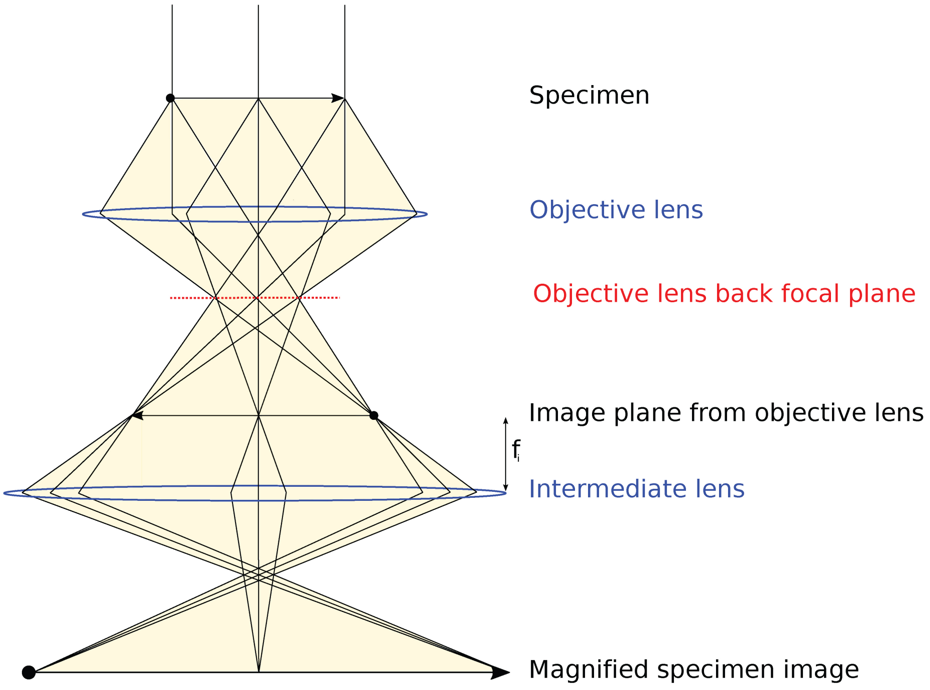

Figure 3.2: Image mode ray diagram of a simplified TEM consisting only in two lenses, objective and intermediate. Condenser and projector are not relevant in this explanation on how the image is formed.

In this mode the image is formed with the electrons transmitted and diffracted through the sample and for this reason the final image will show little contrast between the different crystallographic parts of the sample. What distinguish the different points in the back focal plane are that all the rays diffracted in the same angle are focused into the same point. It can be seen that each point in the back focal plane have rays coming from all the parts of the sample, which means that not all the rays in the back focal plane are required to form the image, generating the image with different types of information and making a poor contrast. Nevertheless, the contrast the contrast in this mode is sensitive to a mass-thickness changes in the sample.

Bright Field

Bright field (BF) is the next observation mode in terms of complexity. In this mode, in order to improve the contrast of the image compared to CTEM, it is used a physical aperture (of few μm in diameter) which is called objective aperture and it is marked in red in Fig. 3.3. It is placed in the back focal plane of the objective lens so it blocks all the electron rays that suffered some scattering after transmitting through the sample.

Placing this aperture avoids the recombination of transmitted and diffracted electrons. The correspondent ray diagram is in Fig. 3.3. In red appears the objective aperture blocking all the rays except the transmitted ones.

In BF the contrast of the image is enhanced compared to CTEM since the darker regions can be understood as a part of the sample that strongly diffracts electrons, giving a useful information about the different features.

Dark Field

The complementary technique to BF is called Dark Field (DF). Fig. 3.4 describes the ray diagrams for both DF and the so called dirty DF.

The main characteristic of this mode is that the objective aperture now only allows to pass a selected diffraction spot from objective lens back focal plane. The image contrast will show bright areas in the crystal that diffracts at the desired angle and dark areas which either does not diffract in the same angle as the aperture or do not diffract at all.

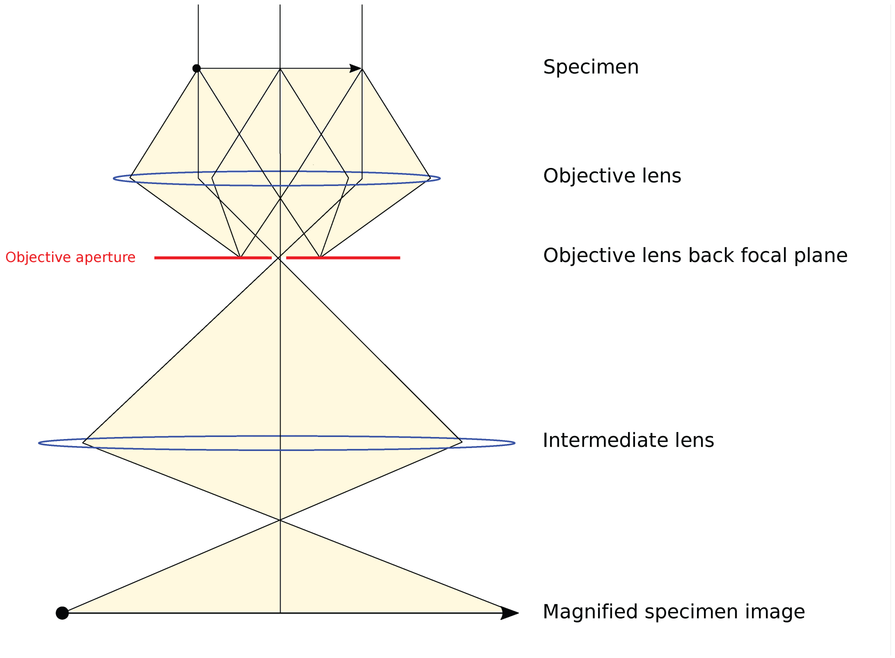

Figure 3.3: Bright Field ray diagram of a simplified TEM consisting only in two lenses. The objective aperture is inserted in order to block all the diffracted rays.

Selecting a diffraction spot far from the optical axis implies that the image is formed by rays that have a big tilt in the intermediate lens, as illustrated in Fig. 3.4 a). Since the electromagnetic lenses from a TEM are far from being in the ideal "thin" lens approximation they are less accurate bending the electrons far from the optical axis. For this reason this mode is called dirty DF. This problem is solved by changing the tilt of the incident electrons in order to have the diffracted electrons close and parallel to the optical axis, as seen in Fig. 3.4 b).

In Fig. 3.4 for better understanding the rays that are diffracted by the sample in the same angle are painted in green. The image is formed only by rays diffracted that specific angle, selected by the apperture.

Selective Area Electron Diffraction

Fig. 3.5 is a ray diagram for the configuration of the TEM in diffraction mode. In this case the intermediate lens is focused in the back focal plane of the objective lens instead of the image plane. Now there is no aperture placed in the back focal

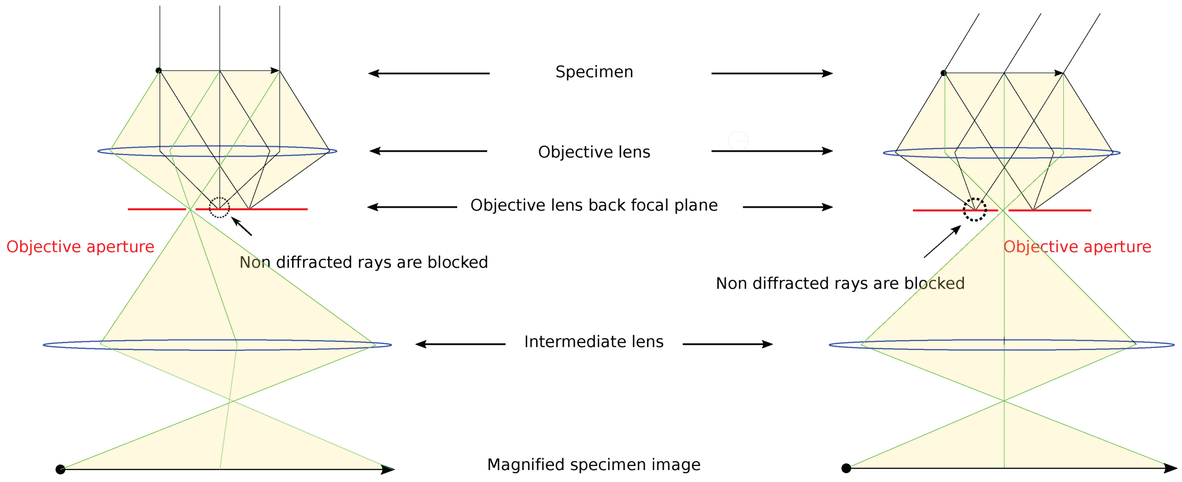

Figure 3.4: Dark Field and Dirty Dark Field ray diagram of a simplified TEM consisting only in two lenses. The difference from both diagrams is the incident angle of the electrons coming to the specimen. In dirty dark field, the left diagram, the incident electrons come straight and forcing the diffracted ray to hit the intermediate lens at a high angle, making it more sensible to aberrations. The aperture is blocking all rays that diffract in a different angle than the objective aperture. In the diagram to the right the incident electrons come from a tilted direction making the selected diffracted ray to pass the intermediate ray through the center.In both images the desired diffracted rays are colored as green so it is easier to follow and confirm that they are the same diffracted beams.

plane as in BF and DF since we use both the transmitted and diffracted electrons to generate the diffraction pattern.

It is common that only a small part of the sample needs to be studied. In this case an aperture is placed in the image plane of the objective lens selecting the area of interest. This technique is called Selected Area Electron Diffraction (SAED).

The study of the diffraction pattern gives essential information and determines the full geometry of a crystalline sample. The angular separation of the diffraction spots gives an inverse proportional measurement of the distance between atomic planes. This relation can be derived by applying simple geometry in Fig. 3.6 and Bragg's law. Bragg's law is:

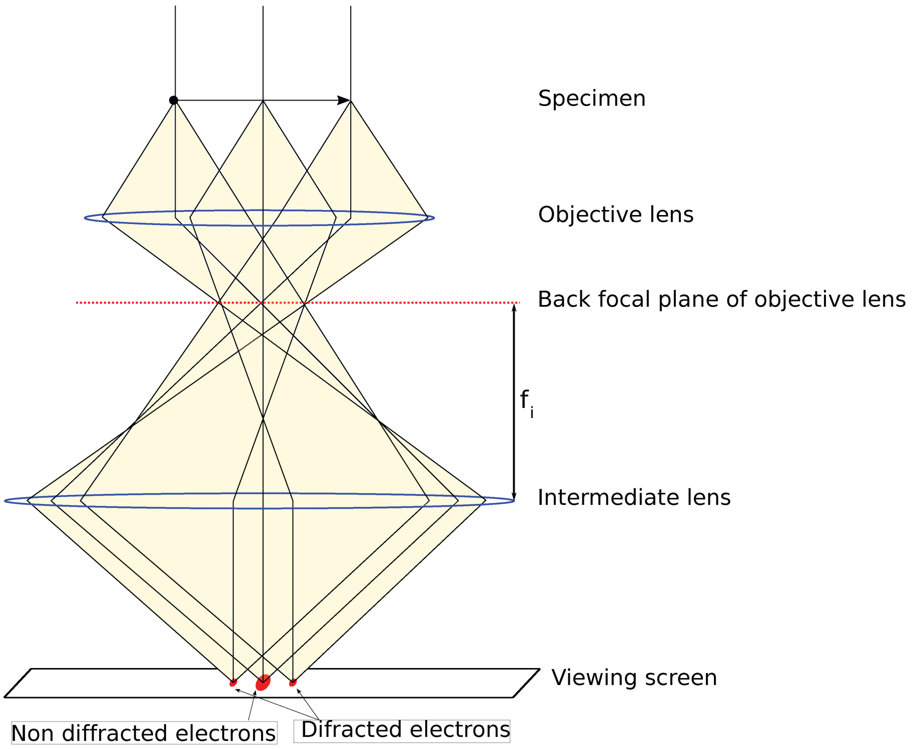

FIGURE 3.5: Electron Diffraction ray diagram of a simplified TEM consisting only in two lenses. The difference between this mode and the previous ones are that the intermediate lens is focused in the back focal plane of the objective lens instead of the image plane.

$$2d\sin(\theta) = \lambda \tag{3.2}$$

where λ is the associated wavelength of the electrons, d is the interplanary spacing and θ is the deviation angle from the electron after the scattering. For the case of small angles eq. 3.2 can be simplified as:

$$d\tan(2\theta)) = \lambda \tag{3.3}$$

Looking at Fig. 3.6 it can be derived:

$$\tan(2\theta) = \frac{r}{L} \tag{3.4}$$

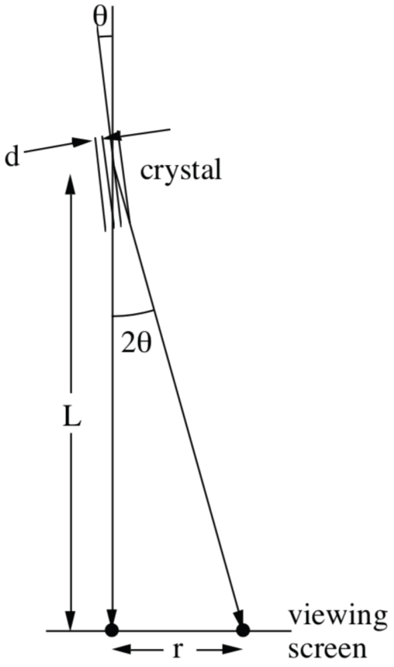

FIGURE 3.6: Geometry used in electron diffraction and definition of camera equation. d is the lattice spacing, θ is the scattering angle, L the distance between sample and screen and r the distance between the the transmitted spot and the diffracted one.

Combining eqs. 3.3 and 3.4 it can be obtained the so called camera equation which relates distances in diffraction patterns in the viewing screen with the interplanary distances:

$$rd = L\lambda \tag{3.5}$$

A more complete way to describe electron diffraction is by using the Ewald sphere construction. The Ewald sphere is an imaginary sphere of radius $1/\lambda$, where λ is the wavelength of the electrons, with the origin of the reciprocal lattice of the given crystal placed at the edge of the Ewald sphere in the direction of the transmitted beam. When the Ewald spheres touches a reciprocal lattice point a diffraction spot will appear in the direction formed by the center of the sphere to that reciprocal point. In electron diffraction this sphere is so large that it can touch a whole plane of the reciprocal lattice, generating its correspondent diffraction spots.

Convergent Beam Electron Diffraction

CBED is a useful observation mode in order to align crystals in TEM. This mode uses a small convergent electron beam, of $\sim$ 100nm, illumination into the sample instead a conventional parallel beam of few μm. Using this condition in diffraction mode enhance the appearance of a set of bands called Kikuchi lines.

Kikuchi lines are caused by multiple scattering events inside a crystal from electrons initially inelastically scattered by atomic planes, where the loss of energy is in the range of hundreds of eV [45]. In reciprocal space Kikuchi lines converge together into crystal high symmetry orientation points, called zone axis, so they are very useful when it comes to align the sample.

High Resolution TEM

HRTEM9 is the technique used if we want to go beyond the diffraction contrast limit in the microscopy used in the previous sections. Here, the image contrast instead of being caused by the intensity of diffracted waves it is caused by the constructively or destructively interference of the phase of the diffracted waves with the transmitted, "showing" points that can be correlated with the atom columns of the crystal. This technique allows to go to magnifications up to 1.2 Mx and it is suitable for the study of atomic defects in crystals and interfaces.

The interpretation of the HRTEM images is not as intuitive as in normal TEM. The contrast in the image is given by the interference of transmitted and diffracted electrons, which can vary to a large degree if the tilt, focus or sample thickness are modified. So in order to talk about atomic positions when analyzing a HRTEM image one should know the previous parameters among other microscope operating conditions.

Scanning TEM

In Scanning TEM (STEM) the microscope is adjusted to do a fine raster scan with a focused convergent beam of electrons (∼0.1 nm) into the sample. The main restriction in this mode is to achieve a small beam size. The quality of the beam will be strongly affected by aberrations in lenses. Similarly to CTEM, STEM generates different types of electrons after scanning the surface. Depending on which ones are studied one can obtain different information form the sample.

High Angle Annular Dark Field STEM
In HAADF STEM the image is formed by electrons that elastically scatter the sample at high angles (75-100 mrad) and collected by an annular detector. In this mode the image contrast can be interpreted as differences in Z number in the atomic columns, and represents a direct map of the elastic scattering power of each atom in the image. This scattering variation is in the order of Z^2.

3.1.2 Electron column

This section describes the main part that form a TEM: the electron column.

- Electron gun

  The electron gun is the part of the microscope that generates a coherent and stable beam of electrons. There are mainly 2 types of electron sources depending on the electron emission principle they use: thermionic and Field Emission Gun (FEG).

  Thermionic emission is based on thermionic effect, the heating of a sharply pointed rod to overcome the electron work function[46]. There are mainly two types of materials that are used in thermionic guns: Lanthanum hexaboride and Tungsten. In the case of the LaB_6 the work function is lower so it is a more efficient material, although it is expensive. In general LaB_6 have a better electron emissivity and lifetime compared to the W ones.

  FEG use the field electron emission to extract electrons from a filament[47]. Electrons now overcome the work function tunneling from the filament by applying a big negative potential, in the order of kV. This guns have a better performance compared with the thermionic ones, creating an electron beam more coherent and smaller in radius with brightness 10 times higher. There are mainly two different types of FEG: cold cathode and Schottky. Cold FEGs extract electrons purely by applying a voltage difference and Schottky uses both thermionic emission and a voltage. The anode is a ring placed beneath the filament and accelerates the electrons.

The energy distribution in thermionic guns is around 2.5 eV whereas for cold FEG is 0.25 eV.

- Lenses and apertures

  Electromagnetic lenses bend the trajectory of the electrons coming from the source and are responsible of focusing the beam into the sample and forming the image. A lens itself is an array of copper wire carefully coiled in a soft iron pole piece. The current running through this coils will exert a Lorentz force to the negatively charged electrons and determine the focal point of the lens, making it relatively easy to modify. Fig. 3.7 a) is an electromagnetic lens of a TEM.

  Apertures are small holes usually in a gold thin film and they can select the angular divergence of the beam and a desired diffracted beam, depending on the needs of the experiment. Their diamater ranges from ∼10 μm to several hundreds. Fig. 3.7 b) is an aperture holder and the typical geometry of the different diameter holes on it.

  A simple version of a TEM consist in 4 sets of lenses and 2 apertures that treat the electrons coming directly from the source down to form a magnified image of a specimen.

  Two condenser lenses and one aperture control the amount of the electrons generated by the source that are used to form the image. This allows to control the beam intensity and tilt to illuminate the sample.

  Two objective lenses and one aperture create the first image of the specimen which will determine the resolution of the final image. The aperture in these lenses is placed in the back focal plane and can select a diffraction or transmitted spot to perform DF or BF.

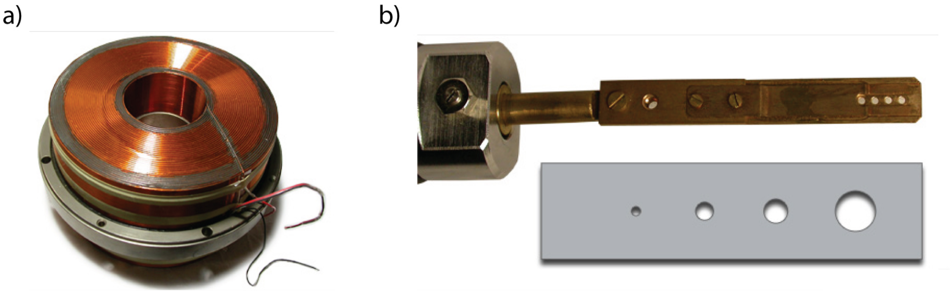

FIGURE 3.7: a) Electromagnetic lens from a TEM. b) On top an aperture holder. On bottom the strip with the different diameter apertures. The smallest one can be 10 μm in diameter. Image adapted from Ref.[48].

The intermediate lens selects the observation mode between imaging or diffraction and magnifies the image created by the objective lenses.

Two projector lenses do a final magnification of the specimen image and projects it to the viewing screen or CCD camera.

- Correctors

  Nowadays lens aberrations are the limiting factor in the resolution HR STEM and HR TEM imaging[49;50]. Aberrations appear in every real lens and are defined as the surface between where the electron wavefront is and where it should be in an ideal lens system. This function can be expressed as a polynomial function where the higher orders are harder to correct. For example the spherical aberration is a third order aberration so it changes with the cube of the electron beam angle with the optic axis.

  The correctors can be placed after the condenser lenses (probe correction) or after the objective lenses (image correction). The schematic shape of the correctors is in Fig. 3.8. They are made up from magnetic poles arranged 3 possible geometries: quadrupole, hexapole or octupole. The quadrupole correct the first order aberrations from the beam and the octupole the third order. A combination of these two can in principle correct different types of aberrations.

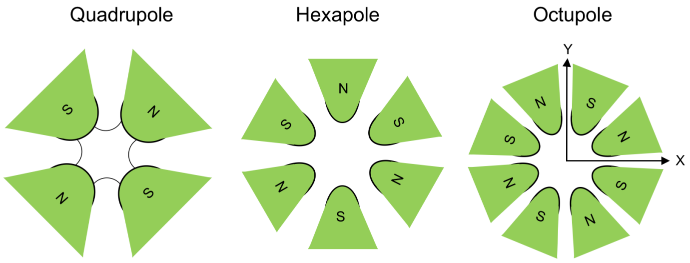

FIGURE 3.8: Multipole lenses that form aberration correctors in a TEM lens.

- Image adquisition

  The most used elements to see the electrons that form the images are fluorescent screens and CCD cameras. Fluorescent screens are used to do quick checks in the microscope and generally to align the sample. When an image is worth to be acquired a CCD camera is deployed in front of the fluorescent screen and saves the image in the control computer.

3.1.3 Vacuum

Good vacuum conditions are mandatory in TEMs. A system of different pumps maintain vacuum levels below specific safe levels for the equipment. A usual safe pressure inside a TEM is $\sim 10^{-5}$ Pa. When a sample is inserted the volume occupied by the sample and its surroundings must be pump before opening the column valve. A pre-pump is done by a rotator or oil pump until the pressure is low enough for opening the electron column valve, where a turbo pump keeps the vacuum.

3.1.4 TEM alignment

The first thing to do when doing a microscopy session of VLS wires is to properly align the sample to a high order zone axis. The steps to do this are described in Fig. 3.9. The main idea is to do CBED of the region of interest and tilt the sample into the direction were the Kikuchi lines meet into a point, called zone axis or a high symmetry orientation. In Fig. 4.3 c) spreaded diffraction spots are obtained by focusing the beam into the crystal, giving rise to Kikuchi lines pointing to a zone axis. Since Kikuchi lines are caused by inelastic electron scattering they do not show too much contrast in thin samples when acquiring the image in the TEM. In this case Kikuchi lines in Fig.3.9 are pointing to the top right corner of the image where there is a high symmetry zone axis.

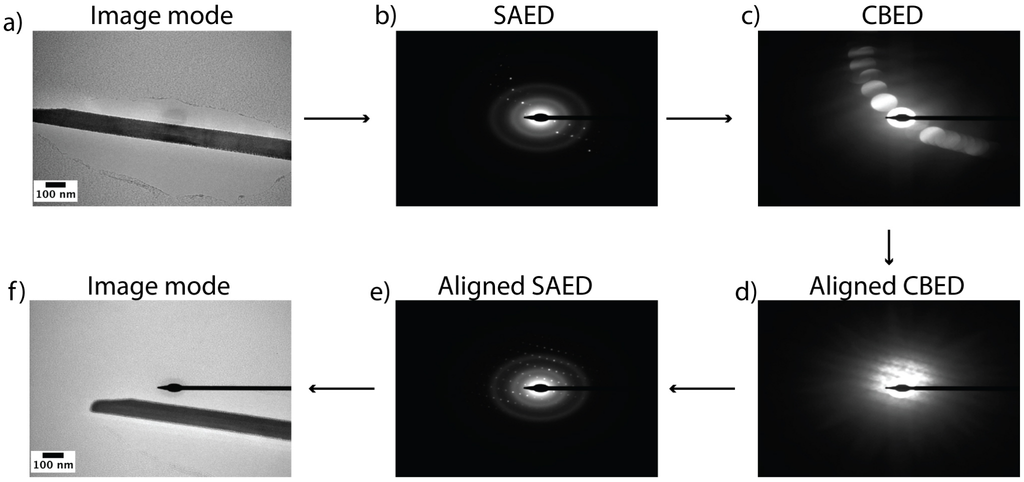

Figure 3.9: TEM images to show the steps in order to align a crystallyne sample when doing TEM. **a**) Image mode of the bottom part of a NW that we want to align before doing the microscopy session. **b**) SAED from the NW from a). **c** CBED from the SAED in b). **d**) CBED after tilting the sample, where the zone axis is now aligned with the transmitted spot. The zone axis was 3° away from the sample position in c). **e**) SAED from the image d). f) The sample is now aligned in zone axis.

3.2 Microscope types

FEI-Philipps CM20

FEI-Philipps CM20 is a TEM with a maximum acceleration voltage of 200 kV with maximum magnification 750 kx and point resolution of 0.27 nm. The system is equipped with a LaB_6 thermionic electron gun and an Energy Dispersive Spectrometer system that allows to perform compositional analysis of the sample. The specimen holder is a double tilt with ± 20° range. Fig. 3.10 is an image of the microscope.

Figure 3.10: FEI-Philipps CM20 TEM in the Niels Bohr Institute, Copenhagen.

JEOL 3000F

The JEOL JEM 3000F is a HR TEM with a 300 kV maximum acceleration with a FEG electron gun. The point resolution is 0.17 nm and has an information limit below 0.1 nm. Since this is a HR TEM the aberrations are the resolution limiting factor with an spherical aberration coefficient of 0.6 mm. The specimen holder has a double tilt range of 25° and the camera is a 2k × 2k CCD camera. It is possible to use a SemiSTEM unit to perform Energy Dispersive X-Ray (EDX). Fig. 3.11 is an image of the microscope.

FEI Titan Low-lase

The FEI Titan Low-base is a HR STEM with spherical aberration correction. The Low-base version has this corrector in the condensor lens, making it a probe corrected TEM, unlike the High-base version which has the corrector in the objective lens making it an image corrected TEM. This microscope is specially designed and equipped to perform HAADF-STEM and EELS. Its maximum acceleration

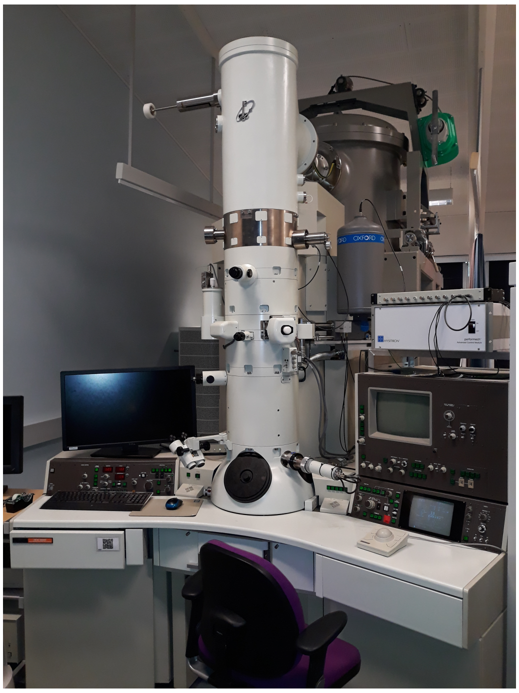

FIGURE 3.11: JEOL 3000F in the Wind Energy Departement from the Danish Technical University, Roskilde.

voltage is 300 kV and the point resolution is 0.09 nm. Fig. 3.12 is an image of the microscope.

FIB

Focus Ion Beam is a technique used for sample preparation for TEM study. The study of planar structures like Selective Area Growth NWs implies to perform cross sectional thin cuts in the growth substrate. This is done by using a focused beam of Ga^+ ions to mill the surroundings of the region of interest and lifting off the lamella, which will be glued into a half moon TEM grid. Fig. 3.13 b) is the schematic functioning mode of a FIB. This lamella containing the sample is then thinned in repetitive steps to a thickness where it becomes transparent to the electrons in the TEM. Fig. 3.13 c) is an example of a lamella thinned to TEM requirements in the center where the SAG NWs are. Fig. 3.13 a) is a Zeiss 1540 XB crossbeam used for the preparation of SAG NWs lamellas for TEM. It has 1 nm resolution in both SEM and FIB microscopes and 5 nm machining resolution.

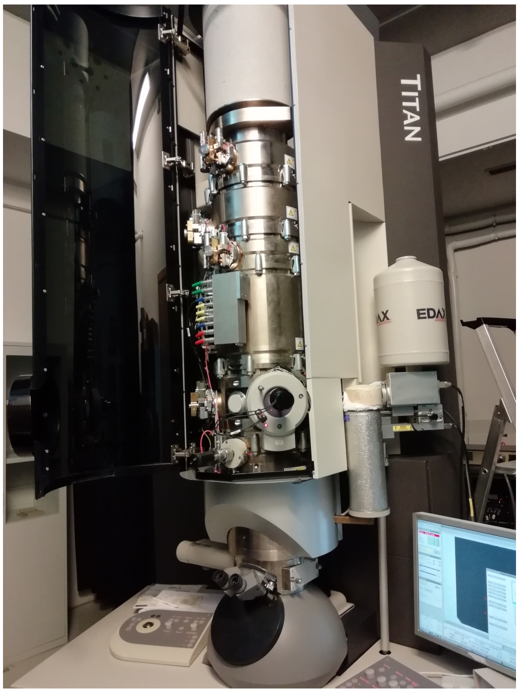

Figure 3.12: FEI Titan Low-base in Laboratorio de Microscopia Avanzada, Zaragoza (Spain).

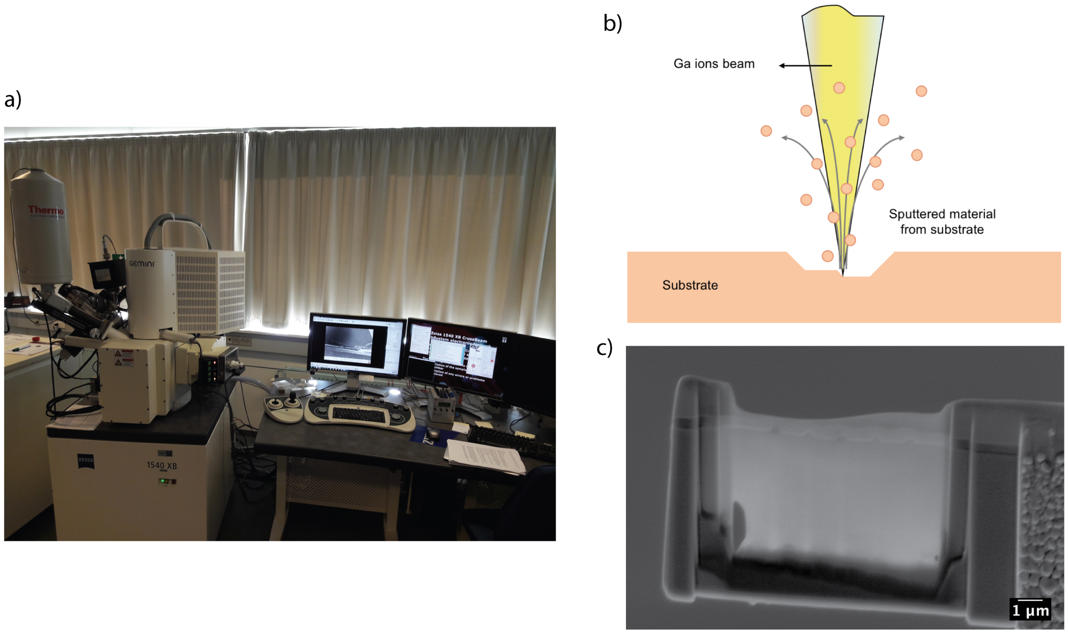

Figure 3.13: **a**)Zeiss 1540 XB crossbeam used for the preparation of SAG NW lamellas. **b**) Schematics of the working procedure of a FIB. **c**) Example of a SAG lamella. The central part is thinned to ∼50 nm. Lamella done by Laura Casado.

Results and Discussion 4

This chapter contains the results obtained and it is mainly divided in 2 different sections:

- The first section is related with TEM results from InAs VLS NWs. It will be shown the different crystallinity types of NWs, wurtzite (WZ) and zincblende (ZB), and the most common defects that can appear on them: stacking faults, twin planes and transition planes from WZ to ZB. As well it is studied the quality of the Al deposited in-situ after the NW growth on different facets in order to create epitaxial hybrid structures of superconductor-semiconductor (SU-SE).

- The second section will focus on the characterization of SAG NWs. The study of these NWs in a TEM was done by performing FIB cross sectional cuts in the desired NW orientation. It will appear as well the different defects that are generated in these structures. The epitaxy between the Al and the GaAs, in order to create hybrid structures, is studied extensively. As a final result, Geometric Phase Analysis (GPA) is done into the interfaces between buffer-NW and NW-Al in order to see the strain generated in the structure caused by the different lattice mismatch parameters and to highlight the misfit dislocations generated in the structure.

All the NWs measured in this thesis were grown by Peter Krogstrup's team at the Niels Bohr Institute in a Varian GEN II MBE system.

4.1 Vapour-Liquid-Solid (VLS)

Fig. 4.1 shows the schematics of the VLS growth process. The basics are that a vapor flux of atoms are collected by a liquid droplet that act as a catalyst, in the case of the NWs studied was gold. This flux of evaporated atoms, which in this thesis are usually In and As, supersaturates the liquid phase either by direct arrival into the liquid phase or by diffusion through near areas around the NW, forcing the droplet to nucleate a layer of the evaporated atoms. The repetition of this process generates an elevation of the catalyst on top of the subsequent nucleated layers of atoms which will create a NW. The usual growth directions for NWs is [111]/[0001] in cubic and hexagonal coordinates for both ZB and WZ showing 6 facets (hexagonal cross section) pointing in the directions $<11\bar{2}>/<1\bar{1}00>$. The substrate used for growing the VLS NWs from this thesis was InAs with (111)B orientation for the NWs in section 4.1.1 and InAs with (100) orientation for the NWs in section 4.1.2.

There are two different techniques to deposit the gold droplets in the substrate before growth and thus the location where the NWs will be created. The first one appears in Fig. 4.2 where the gold droplets were deposited randomly into the substrate. This procedure is faster but it is lost a high degree of control in the sample growth, since the diffusion areas from each wire are not controlled and the size of the droplets have a size distribution, which to a high degree will determine the thickness of the NW. The other technique is to selectively deposit the gold droplets in size and position by processing the substrate before growth, as can be seen in the right image of Fig. 4.2. This process implies the deposition of a mask and selectiveley open windows where the Au will be deposited. This method is more controllable as it shows trends in NW growth depending on the diffusion

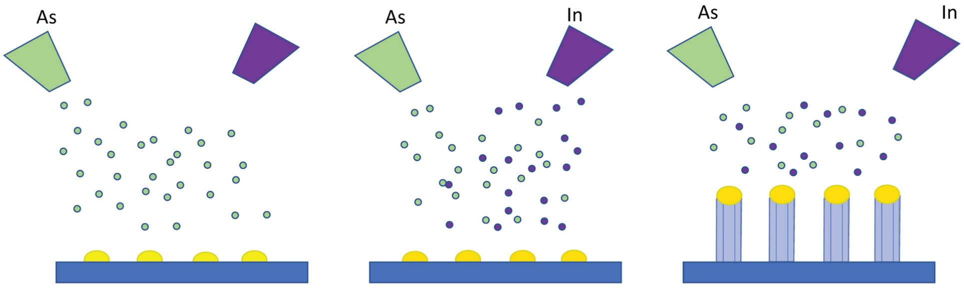

FIGURE 4.1: Basics of VLS growth mechanism. **a**) The catalyst gold droplets are deposited into the substrate are saturated with the group III atoms. **b**) The flux of group V vapor starts in order to supersaturate the Au droplet. **c**) The gold droplet supersaturates and the NW starts growing creating crystal layers perpendicular to the substrate.

area, control the thickness of the NW and grow the NWs only in determined parts of the substrate.

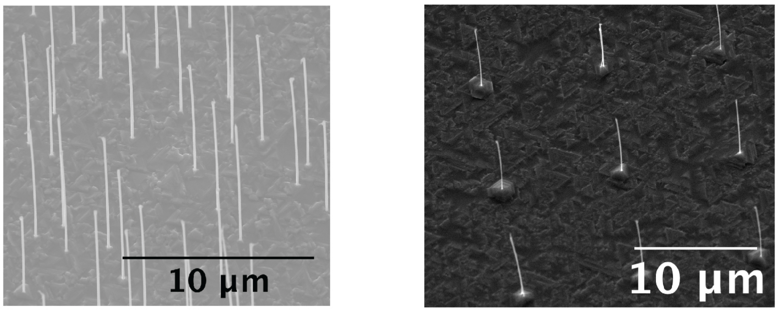

FIGURE 4.2: Tilted SEM images from substrates with positioned and non positioned NWs. In the left image InAs NWs are grown in a substrate within a distribution in position and size of Au droplets. In the right image the same type of NWs are grown in a controlled position.

4.1.1 Defects in VLS NWs

Crystal defects appear not only in the Al but in III-V NWs as well. The most common are coherent planar defects such as stacking faults and twin boundaries, which imply a low surface energy in the interface in comparison with the incoherent boundaries. All these defects appear in the growth direction, [111]/[0001] for ZB and WZ.

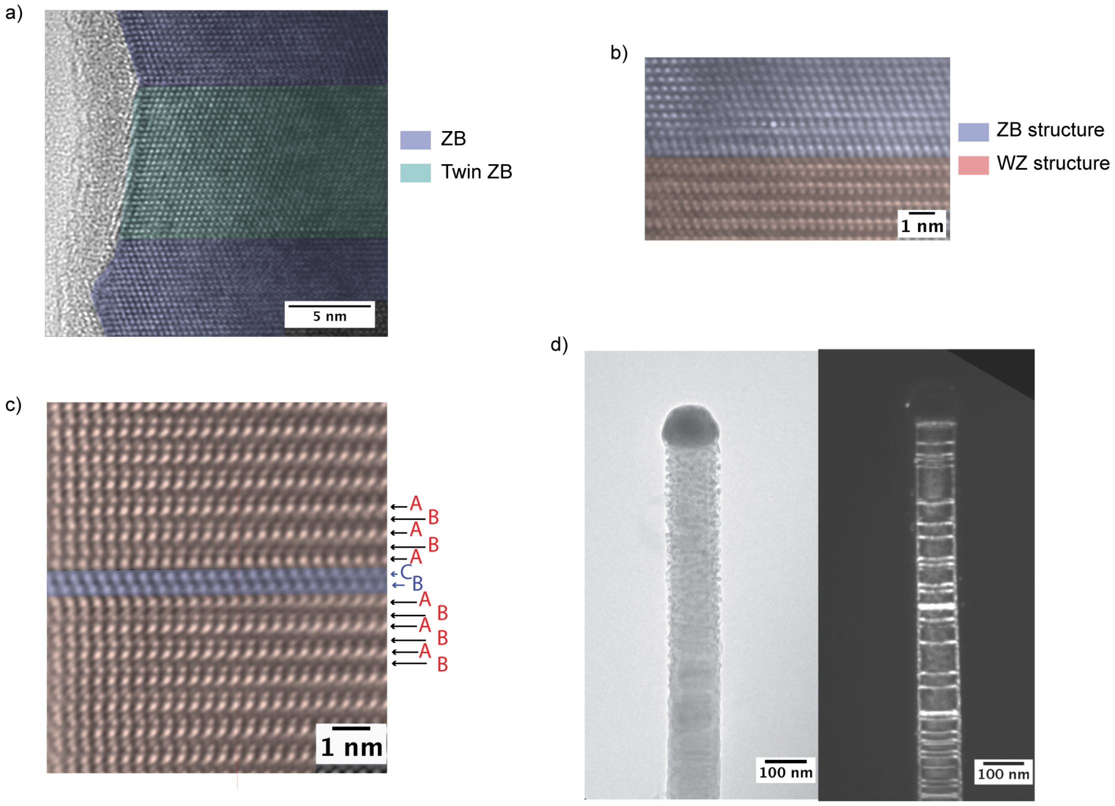

Figure 4.3: HRTEM images showing defects in VLS NWs. **a**) ZB twin crystal with an atomic coherent boundary in a InAs$_{1-x}$Sb$_x$ NW. Highlighted in light blue the twin crystal from the darker blue region. **b**) Crystalline transition from WZ to ZB in the growth direction in a single atomic plane. **c**) InAs NW with a stacking fault in the WZ sequence, incorporating one B and one C planes from ZB. **d**) BF and DF images of a InAs NW with a high density of stacking faults. Images a) and b) taken with Thomas Kanne.

Fig. 4.3 a) shows a HRTEM image of two twin plane boundaries from a InAs$_{1-x}$Sb$_x$ ZB NW. Ternary NWs like InAs$_{1-x}$Sb$_x$ show different types of crystallinity, alternating from WZ and ZB depending on the concentration of Sb introduced during the growth. For Sb concentrations of $x \approx 0.1$ and smaller the NW has WZ structure. Increasing the concentration changes the structure to ZB multi twining and it becomes pure ZB in InSb[51]. In the upper boundary it is clearly seen the different angle in the facet between the normal and twin ZB, $(11\bar{1})$ and (001) respectively.

It also exist coherent transition from WZ to ZB and it is shown in Fig. 4.3 b). The HRTEM image is from an $\mathrm{InAs}_{1-x}\mathrm{Sb}_x$ NW and exhibits a coherent boundary transition between ZB structure and WZ structure.

The HRTEM image from Fig. 4.3 c) show a stacking fault in a InAs NW, the most common crystal defect in VLS wires. The stacking sequence in the lower part follows the common WZ ABAB when two ZB planes BC are introduced in the sequence, to continue later again with the A-B from WZ. The position from the vertical atomic planes in the lower WZ region is displaced 2/3 of a lattice parameter with respect the upper WZ as a result of the two introduced ZB layers.

Fig. 4.3 d) are a BF and DF images of the top part of a same InAs NW. The DF was done with a diffraction spot that highlighted the stacking faults. This method is very useful to detect stacking faults since they have a big diffraction contrast.

4.1.2 Epitaxial Al on InAs VLS NWs

Creating a good epitaxial match between the superconductor (Al) and the semiconductor (InAs) NW is essential in order to fabricate hybrid materials. The sample from Fig. 4.4 are positioned InAs NWs grown on a (111)B InAs substrate with 2 out the 6 facets of the NWs covered with Al of around 8nm in thickness. Image a) is a SEM image of the substrate where it appears the slight bend of the NWs towards the left, caused by the lattice mismatch between the Al and the InAs. The NW bending towards the Al implies that the Al exert a compressive force in the interface. The plane spacing for the InAs and Al planes which form the interface in the simulation from Fig. 4.4 d) is 7.16 Å for the (0001) planes and 1.64 Å for the (111) planes, respectively. This lattice constants are taken from bulk values.

Fig.4.4 c) is a HRTEM image of the interface between the InAs and the Al. In this case the Al has a thickness of 8nm plus 2nm of amorphous native Al oxide developed once the sample is taken out from the MBE. It can be seen that the Al

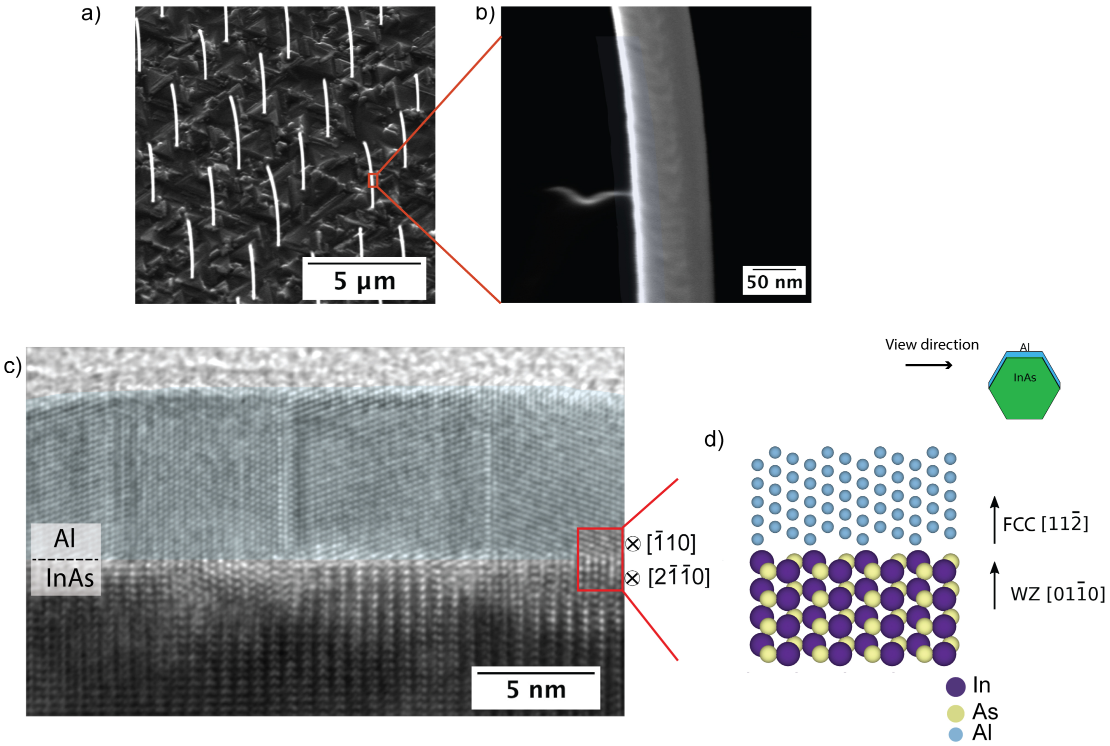

FIGURE 4.4: Epitaxial growth of the Al deposited in-situ on two facets of InAs VLS NWs. **a**) SEM image from the growth substrate with positioned NWs. There is a bending of the NWs towards the left caused by the Al lattice mismatch with the InAs. **b**) SEM image showing the Al deposited in one of the facets of the NW. Al highlighted in blue. **c**) HRTEM image of the interface of the interface between the InAs NW and the Al (highlighted in blue). It can be seen the perfect epitaxy of the Al as well as three coherent twin plane boundaries. **d**) Atomic model from the boundary between the InAs and Al. Lattice parameters taken from bulk values. This sample was provided by Rawa Tanta.

prefers to grow epitaxially from the NW in the $[11\bar{2}]$ out of the interface plane.

A possible explanation for the creation of Al twin planes in this sample is discussed here. The deposition of the Al is done at low substrate temperature, ~ 30 °C, compared with the semiconductor growth regime, ~ 500 °C. This low temperature initiate a formation of small Al islands as the adatom mobility is low at this temperature. When these islands grow enough to merge into a film the orientation they will have is determined by the minimization of surface energy.

FCC metals tend to form a low surface energy (111) out of plane grains[52;53]. In the case of Fig. 4.4 the grains grow in the $[11\overline{2}]$ out of the interface plane, which suggests that for this growth the Al adatoms had enough mobility to create big islands in the beginning of the growth. As the surface to volume ratio of the grain decreases this generates an excess of energy by having big Al islands instead of many of smaller size, and it allows to form Al grains in a less energetic favorable orientation, the $[11\overline{2}]$. After some growth time this islands would merge into a film generating coherent Al twin boundaries. Since this boundaries are coherent, they have a low excess energy density and thus they are very stable, locking the formation of different Al grain orientations.

4.1.3 InAs NWs with Al shadow junction

Other challenge in the fabrication of NWs suitable for quantum transport applications is to create superconductor epitaxial deposition on the facets of a semiconductor NW with regions or islands with no superconductor. Theses islands will behave as Josephson junctions. They were grown in the past by selectively etching the Al but this technique generates a lot of disorder in the Al and InAs. Here I study the crystallinity of NWs with high quality Josephson junctions grown with another approach.

The engineering of such NWs is described in the growth geometry from Fig. 4.5. InAs NWs were grown in a (100) InAs substrate where the gold droplets were deposited in trenches etched into the substrate. The trenches have orientation (111)B and will grow inclined NWs. Once grown, these NWs will be an obstacle to the Al flux coming from the side, as seen in the SEM image Fig. 4.5 b), creating a discontinuous deposition of Al.

Fig. 4.5 c) is a bright field TEM image from 2 NWs 70 nm thick with an Al shadow junction on the left side. The change between the deposition and the junction is sharp and clean, there is no Al deposited in the shadow region. Although the Al seems to have a tail into the shadow region that is oxidized right after leaving the UHV and entering the atmosphere since its thickness is less than 3 nm. The different contrast between the two wires is caused by the slightly different

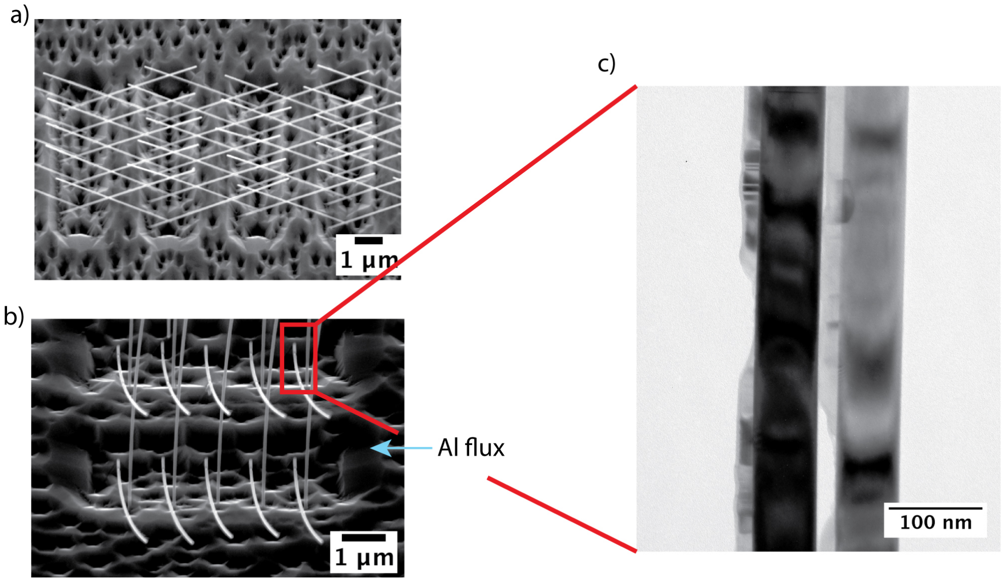

Figure 4.5: NWs grown in substrate trenches to achieve a tilt growth direction, making the NWs to shadow each other when depositing the Al. **a**) SEM front view image of the NWs. **b**)SEM top view image of the growth. The Al flux come from the right allowing the creation of a discontinuous epitaxial film. **c**) TEM image of two NWs. The Al shadow, which is on the left part of both NWs, is clean and has a sharp boundary. Al grains, probably twin planes, are visible in both NWs appearing with different contrast. Sample provided by Sabbir Khan.

crystal orientation. Once one wire is in zone axis, it diffracts more electrons and appears darker, while the other one is brighter and out of zone axis. This sample was grown by Sabbir Khan.

An overview of the quality of the Al deposited in these wires and the different types of grain boundaries is in Fig. 4.6. To understand this image it might be necessary to visualize the electronic version since the atomic planes of the Al might be too thin to be resolved by a printer. In a) there is an atom model of the epitaxy of the Al ($[11\overline{2}]$ out of plane orientation) with a coherent twin boundary highlighted in red where both grains share that column of atoms. Both twin grains, α and β, are indeed the same crystal structure although rotated 180° which is clear in the 3D atom model b). The Fourier transform of the image d) tells that the Al is deposited in a way that there is a perfect epitaxy, since the peaks from the 2

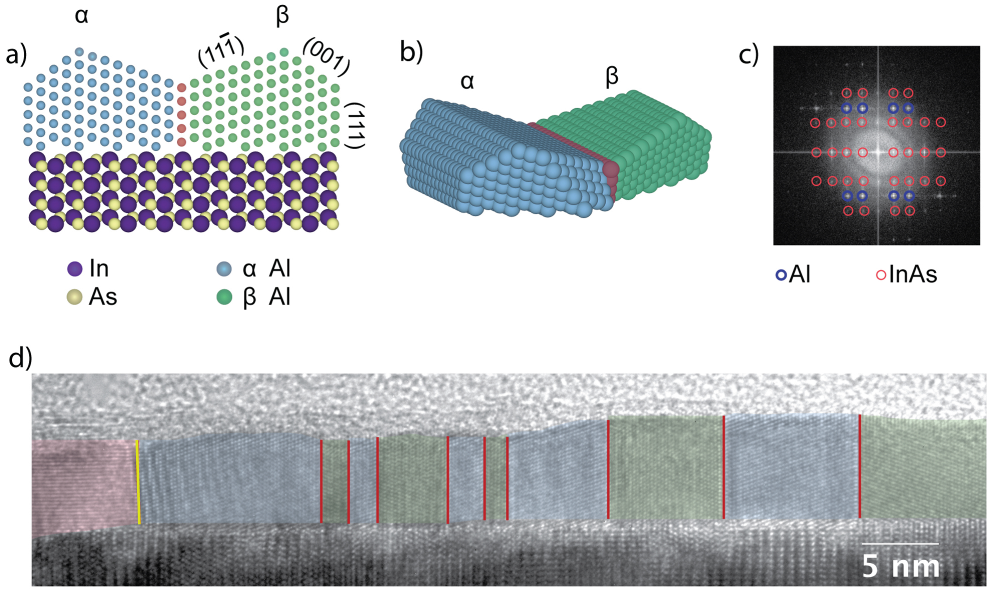

Figure 4.6: Model of the Al deposited in a shadow junction NW. **a**) Atomic model of the epitaxy of the Al and the InAs NW. Blue and green atoms are Al with the [11$\bar{2}$] orientation out of the interface. The red atoms form the coherent twin plane boundary between the grain colored in blue and the one colored in green. **b**) a 3D visualization of the Al with the coherent twin boundary marked with red atoms. The 2 twin grains are called α and β. **c**) Fourier transform of d) showing that the Al peaks (marked in blue) are aligned with the InAs peaks (marked in red) showing a perfect epitaxy of the Al with the NW. **d**) HRTEM image from the interface between the NW and the Al in a region where there is no Al shadow. In green and blue are highlighted the different twin grains of the Al. The vertical red lines denotes the atomic coherent plane twin boundary between grains. The red region corresponds with a [111] out of plane Al grain separated by an incoherent grain boundary.

different phases are completely aligned. This means that the planes have the same orientation, with the characteristic two-to-three bicrystal match between Al and InAs. It appears a series of twin grains in the Al is highlighted in green and blue, in Fig. 4.6 d). Al planes from the coherent boundary marked in red.

A remarkable fact is that in the left part of Fig. 4.6 d) there is a different type of boundary, an incoherent boundary created between the right side Al [11$\bar{2}$] out of plane (blue) and the left side [111] out of plane (red). It is known that the Al out of plane orientation depend on the thickness of the deposition, as stated in Krogstrup et al[25] and discussed in section 4.1.1. The thicker the Al it is, the more common to find it in the $[11\overline{2}]$ out of plane orientation with the different grain twinning. In the case of Fig. 4.6 d) it can be seen both types of Al in a deposition of 8 nm thick. A possible explanation for this is that the mobility of the Al adatoms in the first stages of the deposition in this sample was slightly lower than in the sample from section 4.1.1. This effect might create islands of different initial size before merging together in an Al film. The smaller islands can become [111] out of plane orientation grains whereas the bigger ones, most of the grains in image 4.6 d), develop a $[11\overline{2}]$. Unlike coherent boundaries, incoherent ones have a high excess energy density which implies a big force from the Al crystal trying to put that grain into a lower energy state.

Nevertheless, in order to make solid conclusions about Al mobilities just by looking at the grains it is necessary at least to look a larger section of the wire. The formation of a [111] grain boundary might be a small probabilistic effect along the NW.

4.2 Selective Area Growth (SAG)

SAG is a growth technique that aims to fabricate NWs in a scalable reproducible way. In Fig. 4.7 a) appears the steps used in order to grow a SAG NW sample. Unlike the VLS method where gold droplets are deposited and used as catalyst, SAG uses top-down lithography to define opening windows to the substrate in a previously deposited mask. This fact makes the technique more versatile in comparison with VLS and allows to create more complex NWs and networks of III-V semiconductors. For this technique the common type of substrates is GaAs (001).

Fig. 4.7 b) shows the typical composition of a growth cross section. The first step is to deposit the mask, which is 10 nm of Si oxide for the samples that are analyze in this section, and then open windows on it with the desired pattern. The second is to grow a buffer made of GaAs(Sb) (very small dose of Sb during the growth of the GaAs). This improves the elastic strain relaxation of the NW and

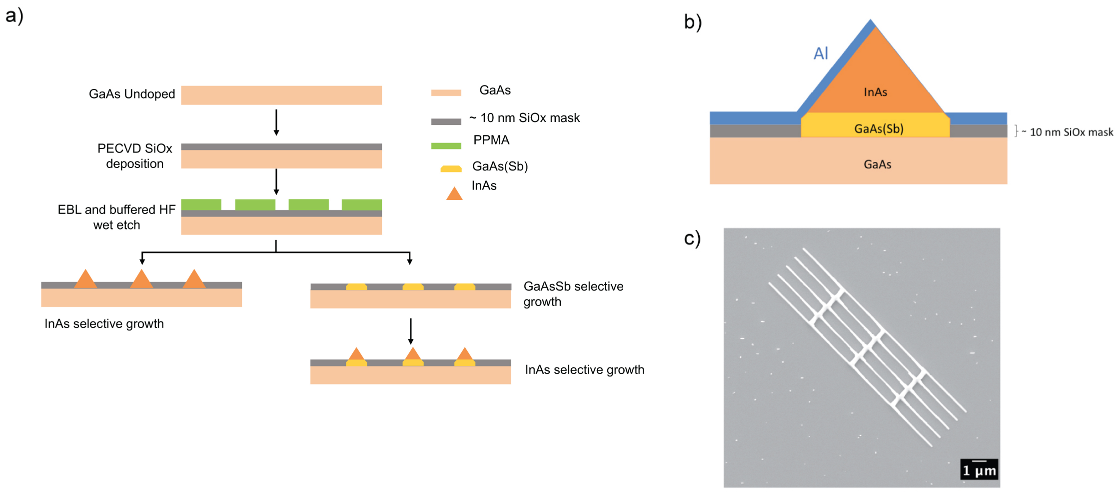

FIGURE 4.7: SAG fabrication process and description of the samples. **a**) Different steps in the fabrication process of InAs SAG NWs with and without GaAsSb buffer. **b**) Cross section description showing the different compositions. **c**) SEM image of an InAs NW network oriented in the [100] direction.

hence avoids the formation of the unwanted misfit dislocations between the buffer and the NW generated by plastic relaxation. After the buffer the InAs NW is grown on top and after a thin Al layer of $\sim$ 8 nm is deposited epitaxially in order to generate the hybrid superconductor-semiconductor structure. Fig. 4.7 c) is an example of a SAG NW network grown in the [100] direction.

4.2.1 FIB lamella

Since SAG NWs are planar structures grown on a flat substrate it is not as straightforward to study its crystallinity in a TEM as it is with the VLS NWs. For this reason it is necessary to perform a cross sectional cut on the NWs to be studied. This is done with a FIB which uses Ga ions in order to get a thin lamella, a sheet of the specimen of less than 200 nm in thickness which will be suitable to study in a TEM.

In Fig. 4.8 it is shown how it looks a FIB lamella, from a perpendicular cut in a SAG NW network. The network consists in 5 interconnected NWs along the $[1\bar{1}0]$ direction.

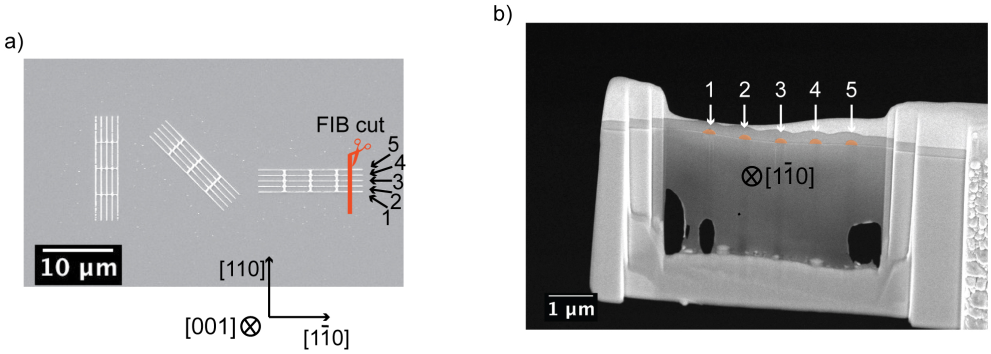

Figure 4.8: FIB lamella perpendicular cut from a NW network oriented in the [1$\bar{1}$0] direction. **a**) SEM image of the NW network used to perform the FIB perpendicular cut, along the red line. **b**) SEM image of the FIB lamella. The NWs labeled from 1 to 5 are highlighted for better visualization. This lamella was done by Laura Casado.

It can be seen in the FIB lamella the thickness differences between the edges and the center, where it approaches a thickness so small that it has some hollow parts in the bottom of the central bottom part. As well its darker color in the center means that it is so thin that some SEM electrons transmit through it giving a lower contrast. The enumerated NWs in Fig. 4.8 a) corresponds to the enumerated NWs in b) which are highlighted in orange for better visualization since they are small compared with the whole lamella.

4.2.2 Epitaxial Al on InAs SAG NWs

Achieving a perfect epitaxy between the SAG semiconductor InAs and the superconductor Al is a major objective in order to create hybrid materials for quantum transport. In this section this will be studied by doing aberration corrected HAADF STEM to the InAs NW number 4 from 4.8 b). Fig. 4.9 a) shows a HAADF STEM image of the NW in the [1$\bar{1}$0] zone axis with the buffer and the NW highlighted in different color. The Al source is tilted at a certain angle so it only gets deposited in the [11$\bar{1}$] and the top part, leaving the [111] facet clean (see orientations in Fig. 4.9 a)). Unlike the InAs VLS NWs, InAs SAG NWs grow in ZB structure.

Fig. 4.9 b) is a magnified HAADF STEM image from the green rectangle in

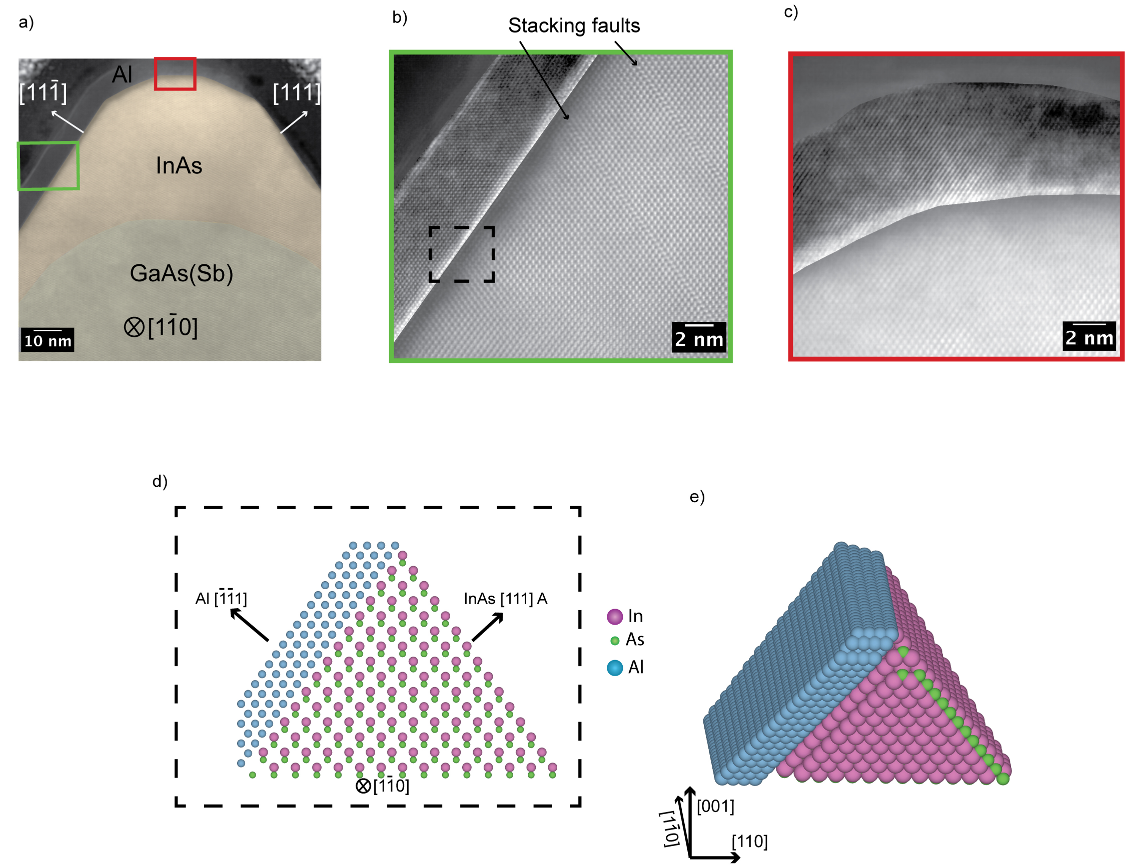

FIGURE 4.9: Epitaxy of the Al deposited in a SAG NW. **a**) HAADF STEM image of a cross section SAG NW along the $[1\bar{1}0]$ zone axis. In the lower part there is the GaAs(Sb) that separates the InAs (on top of the buffer) from the substrate. The facets of the NW are $[11\bar{1}]$ and $[111]$ with the Al deposition on the top and left facets. **b**) HAADF STEM image from the green rectangle in a). The Al has an epitaxial growth from the $[11\bar{1}]$ NW facet. **c**) HAADF STEM image from the red rectangle in a). Both in b) and c) the contrast of the Al was enhanced with a software to improve visibility. **d**) Atomic model of the Al epitaxy from the dashed region in b). **e**) 3D model of a NW with an Al deposition showing the spacial orientation and symmetry of the sample studied in this figure. Images a), b) and c) taken with Sara Martí Sánchez at LMA (Zaragoza).

a). Since this observation mode is highly sensitive to the atomic number Z the Al appears darker than the heavy atoms In and As. For this reason the contrast in the Al deposition has been locally increased to make easier the observation. The epitaxy along the interface of the NW is perfect and the Al is monocrystal along all the $[11\bar{1}]$ facet. Even at the top facet the Al maintains the same crystal structure again with a perfect epitaxy, as seen in Fig. 4.9 c) which is a high magnification from the red rectangle in a). Note that even in the SAG technique the NWs form coherent planar defects like stacking faults, showed in Fig. 4.9 b). Two atomic models simulate the interface between the epitaxial Al and the $[11\bar{1}]$ facet from the NW in Fig. 4.9 a) and b). The first one is a front view of the interface in the $[1\bar{1}0]$ zone axis and the second one is a 3D view of the interface to make an idea of the 3D view of the structure.

4.2.3 GPA strain analysis

GPA is one of the most effective tools when it comes to study internal crystal strains and more complete and powerful in terms of results than other similar techniques like Peak to Peak Analysis. Applying GPA to a TEM FIB lamella of a NW gives information on the strain in the crystal and the expansion and contraction of a desire set of planes compared to an arbitrary defined non strained region.

In order to obtain a complete information about the NW studied in the previous section, the GPA method was applied to a set of two different sets of planes which are specified in Fig. 4.10 b). The InAs (110) planes are the vertical planes from the NW, perpendicular to the interface between the buffer and the NW, so they provide a valuable information about the strain relaxation method. The (111) planes will provide as well useful information since it is the growth direction.

Fig. 4.10 c) and d) shows the dilatation and rotation map of the (111) and (110) planes of the NW. In these two images the buffer is taken as reference of unstrained region, so all the dilatation and rotation values in the InAs are a comparison with the GaAs(Sb). As a first approach in both dilatation maps it can be seen that the InAs (111) and (110) planes are around a 6% expanded, where the theoretical lattice mismatch between InAs and GaAs(Sb) is 7%[28].

Fig. 4.10 e) shows a strain profile along the dashed line in the dilatation map from the (111) planes. In the profile the are 3 different regimes that are visually fitted with the purple, green and red lines for clarification. The strain relaxation process takes place basically in 2 different regions, the green and the purple lines. The red line has 0 slope meaning that the buffer is completely relaxed and that the NW does not have any influence on it since it is much smaller. After the transition to the NW, in the first 20 nm, there is a region with a high change in the dilatation. This implies that the NW relaxes faster in the area closer to the buffer. Then it continues relaxing at a smaller rate in zones closer to the top, described with the purple line.

A possible explanation for the dilatation taking place in two differentiated regimes in the profile in Fig. 4.10 e) and the fact that it does not reach the 7% on the top of the wire is described here. It is likely that the NW is globally compressed in the axial (110) planes. A way to prove a global NW compression would be to perform a longitudinal FIB cut (instead of a cross sectional) GPA strain analysis in this NW and check if this axial compression create a longitudinal expansion of the $[1\bar{1}0]$ planes, in consistence with the crystal Poisson's ratio. This axial compression might explain why the NW structure is not relaxed in the top, far from the interface, but not the change it the relaxation slope. The fact that the NW relaxes faster in regions closer to the interface might be induced by compositional reasons. If some Sb from the buffer or the substrate diffuses into the NW at the first stages of the NW growth this will have an implication on its relaxation, behaving in a different way as in the case of having a clean interface from GaAs(Sb) to InAs.

Another remarkable result is the appearance of a periodic array of points which concentrate a high strain in the left part of the interface in both dilatation and rotation maps. This points correspond to misfit dislocations and are caused by a plastic relaxation of the crystal. The existence of this incoherent defects lower the performance of these NWs when running quantum transport experiments[54]. In the (111) planes dilatation map (Fig. **??**) it is seen that the strain in the left part of the NW with reddish colors is smaller compared with the right one with yellow predominant colors. A possible explanation for this can be that the relaxation mechanism of the NW forces it to plastically relax, creating misfit dislocations, and thus minimizing the overall strain of the structure.

Rotation maps show how many degrees are bended the selected planes in comparison with the planes defined by the selected Bragg Peak. In the case of the [110] planes means how much they bend towards the left or towards the right. In both rotation maps can be seen the same trend, the planes bend positively (counter clockwise) in the left part of the NW and negatively (clockwise) in the right part. The explanation is that the NW expands to the sides in order to accommodate the high strain generated in the interface. Again the misfit dislocations are visible as points with a high strain accumulation. The fact that they are a strain release method of the NW the planes do not bend as much in the left part as in the right part, reaching only a bend of around 4° instead of 6°.

The reason why the dilatation and rotation maps for the (111) planes are more noisy than the (110) planes is because the code used to run this experiments is not optimized to differentiate in a direction different than the standard X and Y axis.

The GPA method can also be applied to the Al in order to look for defects. In this case it is known that the Al deposited after the growth is not strain and it plastically relaxes in the surface of the NW. Fig. 4.11 a) shows the part of the NW where it was studied the interface between the Al and the InAs. Image b) shows the epitaxy of the Al as the Bragg Peaks are ordered and placed around the InAs ones. Fig. 4.11 c) is the dilatation map of the Al $(1\bar{1}1)$ planes setting as the reference the InAs $(11\bar{1})$ planes. The Al appears to have the same blue color along the whole deposition meaning that it is not strained. The dilatation has a value of $\sim$-40% which corresponds to the percentage lattice difference between the Al and the InAs. As a result of not being strained it is created a periodic array of misfit dislocations along the Al-InAs interface, marked with yellow arrows.

These dilatations map looks noisy and less accurate than the previous ones probably because the two Bragg Peaks selected (one as reference, the other one the one we wanted to study) are far apart in the Fourier space as seen in Fig.4.11 b). This might induce imprecisions since the gaussian mask that filter the desired frequencies does not conserve the initial intensity of the Bragg peaks.

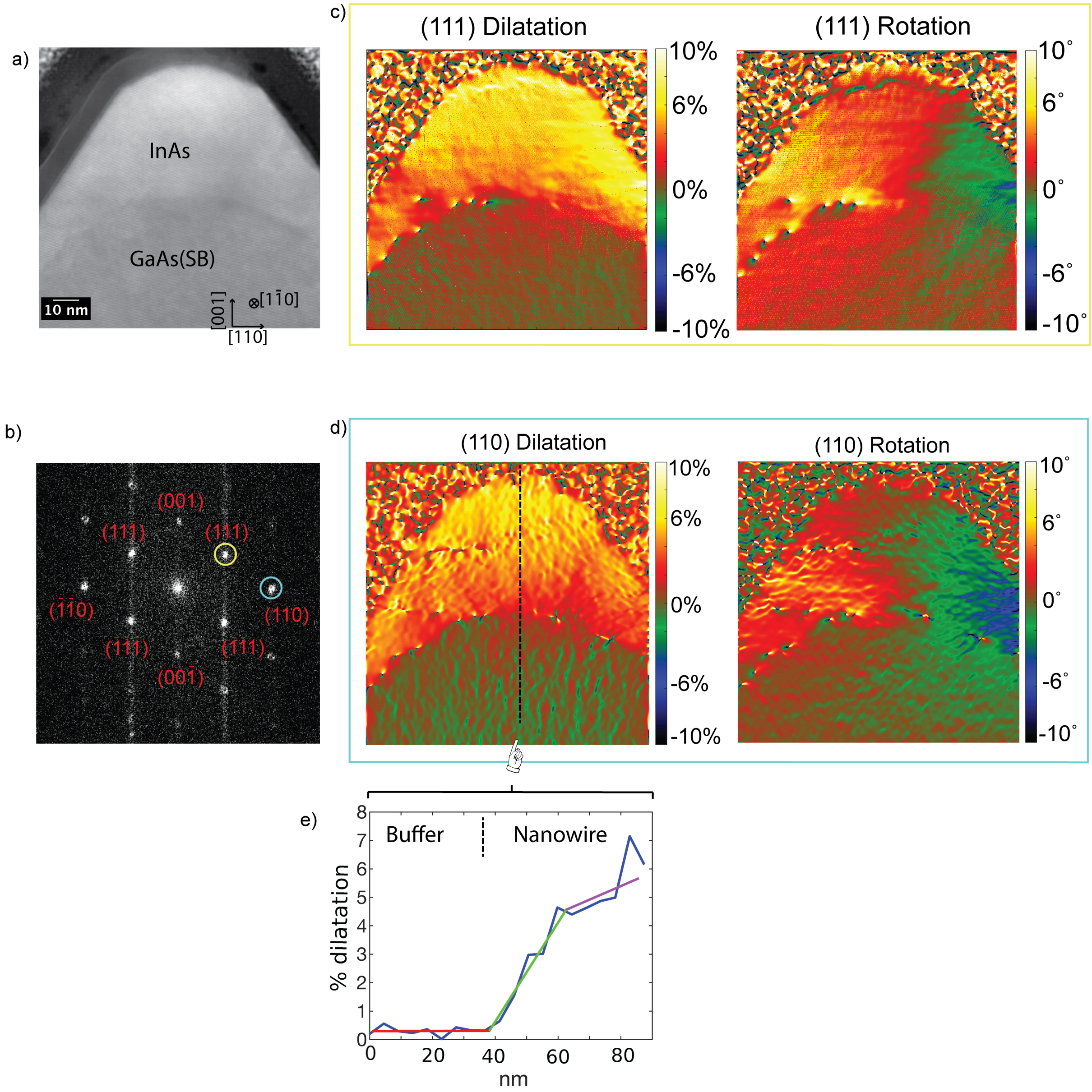

FIGURE 4.10: **a**) HAADF STEM image from the cross section SAG NW studied. **b**) Fourier transform of the image showing the Bragg Peaks used in the GPA analysis. **c**) Dilatation and rotation maps of the (111) planes. **d**)Dilatation and rotation map of the (110) planes. **e**) Strain profile of the dilatation along the (110) planes, from the dash line in image d). The red, green and purple lines are a visual fit just to remark the 3 different relaxation regimes. Image a) taken with Sara Martí Sánchez.

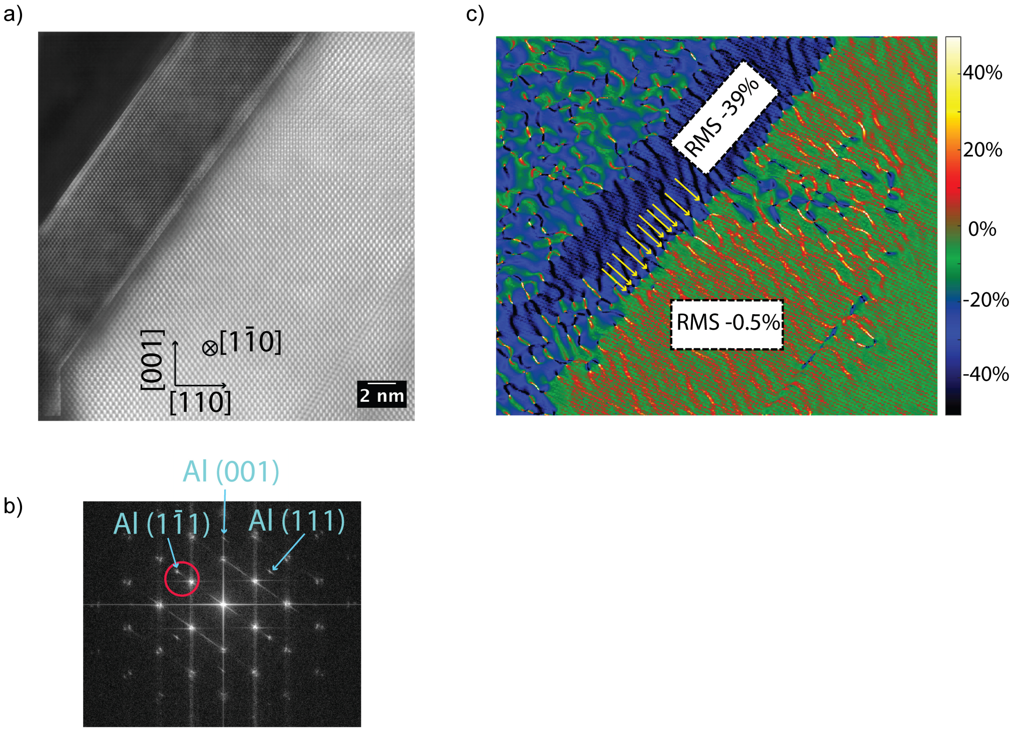

Figure 4.11: Study of the Al deposition on the $[11\bar{1}]$ NW facet. **a**) HAADF STEM image from the bottom left part of the NW. The contrast of the Al is enhanced with a software in order to improve visibility. **b**) Fourier transform with the Al peaks sitting in the same orientation as the InAs in a 2-to-3 ratio, showing the epitaxy of the Al deposition. **c**) Dilatation map of the $[1\bar{1}1]$ planes showing a difference of 40% between Al and InAs. The yellow arrows point to misfit dislocation originated in the interface. Image a) taken with Sara Martí Sánchez.

Conclusions and Outlook

5

This thesis focus on the structural characterization of the interface between InAs and Al in the two different growth approaches VLS and SAG. GPA method was coded in MatLab and applied to the SAG cross sectional cuts.

Conclusions

The Al deposition in VLS wires exhibited a perfect epitaxy with the characteristic 3 to 2 match between Al and InAs, forming a hybrid superconductor-semiconductor crystal. It was found two different Al orientations, the [111] and $[11\bar{2}]$ out of the interface. The grains with the $[11\bar{2}]$ orientation were found more probable and created a coherent grain boundary between twin grains. The fact that [111] Al grains appeared with less probability is related with the energy of the incoherent boundary formed between the [111] and $[11\bar{2}]$ grains and due to the small thickness of the deposition.

FIB cross sectional cuts were performed to $[1\bar{1}0]$ oriented SAG NWs in order to study the structure of the hybrid interface, between Al and InAs. SAG NWs showed as well a perfect epitaxy between the Al and the InAs. The Al formed a single crystal layer deposition along the lateral and top facets. The orientation of the Al was found to be the $[\bar{1}\bar{1}1]$ out of the interface plane. Several stacking faults appeared in the InAs NW in the (111) planes. GPA method was performed into the the HRTEM images in order to extract information about internal strain in the NW and in the interface. The dilatation maps showed a non strained GaAs(Sb) buffer and two relaxation regimes for the NW. In the first 20 nm, starting from the buffer interface, the NW relaxes in a fast way whereas in the top part of the NW relaxes at a slower rate. This might be explained by the accidental incorporation of Sb during the first stage of the NW growth or Sb diffusion from the buffer. Other explanation can be the dilatation of the $(1\bar{1}0)$ planes, the longitudinal planes in the NW, due to Poisson effect. Another result is the identification of misfit dislocations created in the interface between the GaAs(Sb) buffer and InAs NW as a result of the 7% difference in lattice parameter. This dislocations are a strain release method for the NW and have a strong influence both in the dilatation and rotation map as they are highly strained points in the crystal. The GPA applied to the Al-InAs interface showed a -39% dilatation of the Al (in agreement with the lattice parameter mismatch) and a periodic array of dislocations showing a 3 to 2 epitaxy.

Outlook

Future experiments in this topic can help to answer what is the exact mechanism that creates the two different relaxation regimes of the InAs NW on top of the GaAs(Sb) buffer. Knowing this is a key piece in order to eliminate the undesired misfit dislocations. Performing FIB cuts in different directions, like the longitudinal along the NW or the (111) growth direction, might clarify how does the strain distributes and how strong is the Poisson effect. An attractive fact to study is if there is any influence in the NW strain measured in GPA caused by the FIB process, since a lamella containing the sample have two new free surfaces where the NW can relax into. Clear out if this two regimes is caused by undesired Sb diffussion into the NW is desired as well.

Appendix 6

6.1 TEM grids

All the samples were deposited in TEM grids suitable to be inserted into the microscope. The type of grids used during this thesis were the standard FCF200-CU which have a copper mesh and a deposition of 10nm formvar (a type of resin) and 1nm of carbon. Fig.6.1 is an example a TEM grid used to study NWs.

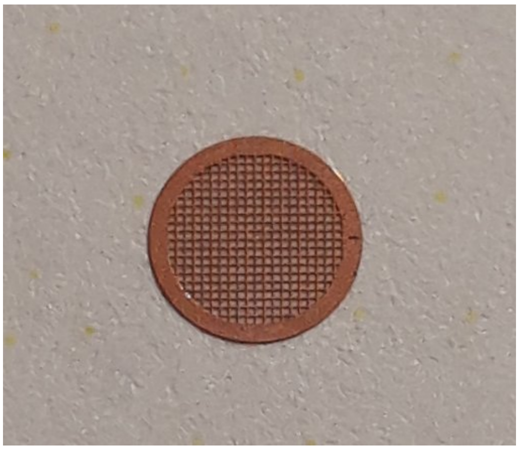

Figure 6.1: Example of a TEM grid used.

6.2 Wire deposition

NWs had to be transfered from the growth substrate into a suitable TEM grid before a microscopy session. Depending on the sample a different method was used. In the next list they are ordered from most to least precise method:

Micromanipulator

The micromanipulator is the most precise way to transfer NWs from the growth substrate to the TEM grid. This set up allows to deposit individual selected NWs although at a high time cost. Both substrate and grid are placed on top of a movable stage with a microscope incorporated. A sharp needle (~100 nm radius at the end) is mounted in a holder that can be controlled with very high precision so it is possible to brake a desired wire and transport it into a desired part of the TEM grid. Fig.6.2 is the set up used.

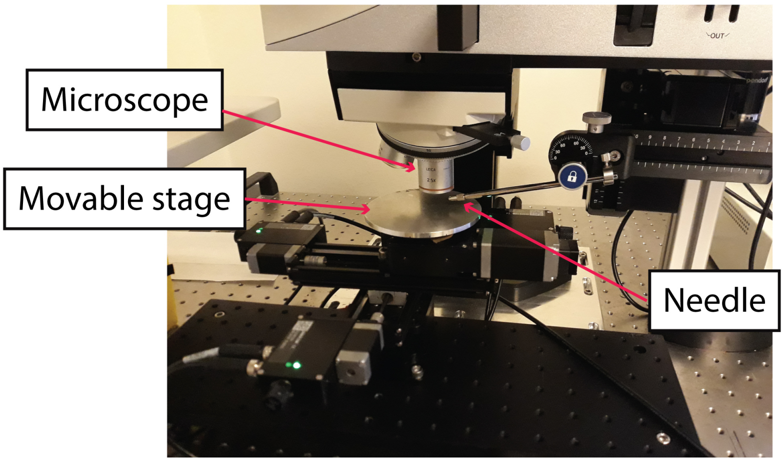

FIGURE 6.2: Micromanipulator used to selectively transfer NWs from the growth substrate to the TEM grid

Direct scratch

This method consists in gently scratch the TEM grid into the growth substrate in order to randomly brake NWs that will eventually get attach in the carbon film. This method is more dirty compared to the micromanipulator although there is some control on the orientation of the NWs deposited. A high number of them will be oriented in the same direction as the scratch was done into the substrate.

Napkin deposition

This method is the least controllable and consists in gently touching the growth substrate with the corner of a clean room napkin. After this, the napkin is gently shacked above the TEM grid. Some NWs will fall into the grid and get attach to it, although there is no control on which ones are or their orientation.

Both direct scratch and napkin deposition are done mainly in samples with non positioned NW.

6.3 Scriber

The scribber is used to cut wafers or substrates from growth samples into smaller parts. It consists in a movable stage with a diamond tip on top. The pressure done by the diamond, the position and length of the cut can be controlled precisely. In Fig.6.3 appears a SAG wafer cleaved into the 9 identical chips that form this growth. The missing chip from the center was the one used to perform the FIB cuts.

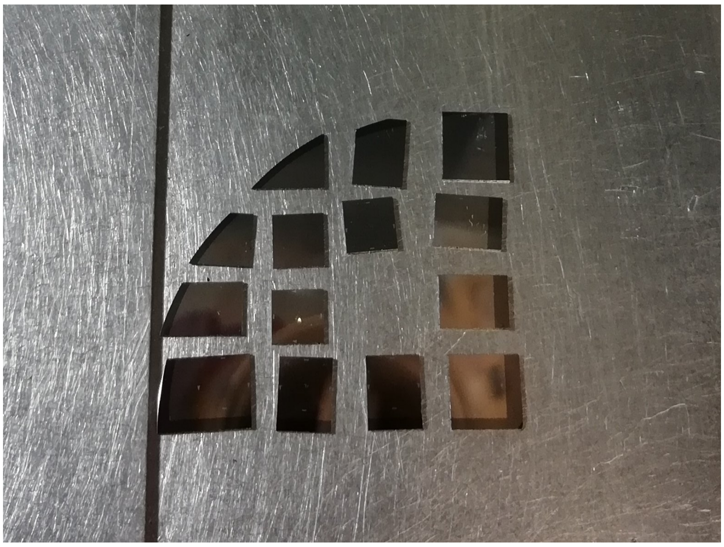

FIGURE 6.3: SAG wafer cleaved into the different chips.

6.4 GPA MatLab code

Although the MatLab code is functional and gives coherent results it is far from being optimized. Nevertheless, it has implemented on it commands and functions to make it as automatic as possible by using prompts and plotting automatically. The time consumption was highly reduced (from ∼ 60 to 2 s) when in the last version of the code was removed the phase unwrapping, which it didn't add any relevant information. The following sections contain the main script and the internal functions created to simplify the understanding while writing the program.

Main code

```
clc
clear all
close all

set(0,'defaulttextinterpreter','Latex')

addpath(genpath('/Users/martinec/Dropbox/Thesis/Simulations/GPA_git_versions'))

[file_name_format,path_folder,image,path_image,image_name,format] = gpa_initialize; % Open image
and create experiment folder

image = image(:,:,1);

image = image - mean(image(:)); % subtract mean value of the image, this will remove the central
peak from the FFT spectra

[path_saved_images,folder_name] = gpa_create_folder(image_name,path_folder); % Creates a folder
where all the images will be saved. Name: original image name + date
[ly, lx, Cx, Cy, image_phase, image_composed, w, image_composed_window] =
gpa_compose_image(image);% Image composition and preliminary treatment. Image compose window is
the image with the Hann mask

FFT of iamge
[Fimage_complex, Fimage_complex_sh, Fimage_amp, Fimage_ph, Fimage_amp_sh, Fimage_ph_sh,
Fimage_amp_sh_log10] = gpa_fast_fourier_transform(image_composed_window);
```

```
[image] = gpa_plot_gray(image,1,image_name,’Original Image’); %Plot of the real image. Title
goes between the ’---’

[power_spectrum_plot] = gpa_plot_gray(Fimage_amp_sh_log10,2,image_name,’Power Spectrum’); %Plot
of the Power Spectrum of the image. Title goes between the ’---’

Coordinates of the FIRST Bragg Peak to get the full displacement

[Fimage_amp_sh_log, cursorpositionx, cursorpositiony] =
gpa_read_braggpeak_coordinates(Fimage_amp_sh); % For reading the coordinates of a point in an
image.
Press space later to get the coordinates as a variable called h

[mass_centered_bragg_peak]=
gpa_center_of_mass(Fimage_amp_sh,lx,ly,Cx,Cy,cursorpositionx,cursorpositiony); %Center of mass
of selected bragg peak .
g = mass_centered_bragg_peak -[Cy, Cx];
g = g./[ly,lx];
[moved_mask] = gpa_gaussian_filter(lx,ly,Cx,Cy,mass_centered_bragg_peak); % Gaussan filter
applyed to mass centered . ASK HERE A PROMPT FOR THE RADIUS OF THE GAUSSIAN FILTER

[plot_filtered_power_spectrum,iFimage_amp_fil,iFimage_ph_fil] =
gpa_inverse_fft(Fimage_complex_sh,moved_mask); % Filter the FFT, unshift and back to real space
[power_spectrum_fil_plot] = gpa_plot_gray(plot_filtered_power_spectrum,3,image_name,’Filtered
Power Spectrum’);

Substraction of the reference region
[phase_mean] = gpa_substraction (g,lx,ly);

iFimage_ph_fil_substracted = iFimage_ph_fil-phase_mean;
iFimage_ph_fil_substracted = mod(iFimage_ph_fil_substracted,2*pi);

[phase_real_space] = gpa_plot_color(iFimage_ph_fil,4,image_name,’Phase in real space’); %

cmap = imread(’colormap_gpa.png’);
cmapd = im2double(squeeze(cmap(10,:,:)));
colormap(cmapd);
colorbar
```

```
displacement = iFimage_ph_fil_substracted./(2*pi*norm(g)); % Here I do the translation from
phase in real space to displacement according with the theory
displacement = displacement-min(displacement(:));

[displacement_in_pixels] = gpa_plot_color(displacement,5,image_name,’Displacement in pixels’);

cmap = imread(’colormap_gpa.png’);
cmapd = im2double(squeeze(cmap(10,:,:)));
colormap(cmapd);
colorbar

%
[p1,p2,p3,zero_strain_region] = gpa_reference;

[normal,plane,im_unwrapped_substracted] = gpa_substraction_plane(displacement,p1,p2,p3);

figure(8)
imagesc(im_unwrapped_substracted)

cmap = imread(’colormap_gpa.png’);
cmapd = im2double(squeeze(cmap(10,:,:)));
colormap(cmapd);
colorbar
daspect([1,1,1])

Dilatation

strain = diff(displacement, 1, 1);  % diff(A,1,1) works on successive elements in the columns of A
                                    diff(A,1,2) works on successive elements in the rows of A
strain = medfilt2 (strain,[3 3]);
figure(9)
imagesc((strain)*100)

cmap = imread(’colormap_gpa.png’);
cmapd = im2double(squeeze(cmap(10,:,:)));
colormap(cmapd);
colorbar
daspect([1,1,1])
```

```
Rotation

strain = diff(displacement, 1, 2);
strain = medfilt2 (strain,[3 3]);
figure(10)
imagesc(strain*100)

cmap = imread('colormap_gpa.png');
cmapd = im2double(squeeze(cmap(10,:,:)));
colormap(cmapd);
colorbar
daspect([1,1,1])
```

Center of mass general function

```
function [mass_centered_bragg_peak] = gpa_center_of_mass(Fimage_amp_sh_log,lx,ly,Cx,Cy,cursorpositionx,

background = zeros(ly, lx);
prompt = '2) What is the radius of the circular mask? Normal values between 5 and 30, depending on imag
R = input(prompt)
circle = fspecial('disk', R);
circl_backgr = imfuse(background,circle);
circ_mask2 = rgb2gray(circl_backgr);
circ_mask3 = circ_mask2./max(circ_mask2(:));
circ_mask = circshift(circ_mask3,[Cy-R Cx-R]);
moved_circ_mask = circshift(circ_mask,[Cy+cursorpositiony-3 Cx+cursorpositionx-3]);
moved_circ_mask = double(moved_circ_mask);
Fimage_amp_sh_log_circ_mask = Fimage_amp_sh_log.*moved_circ_mask;
mass_centered_bragg_peak = centerOfMass(Fimage_amp_sh_log_circ_mask.^2);

end
```

Center of mass

```
function varargout = gpa_centerOfMass(A,varargin)
```

```
narginchk(0,1);
nargoutchk(0,1);
fname = 'centerOfMass';

validateattributes(A,{'numeric'},{'real','finite'},fname,'A',1);

A(isnan(A)) = 0;
if ~(strcmpi(class(A),'double') || strcmpi(class(A),'single'))
    A = single(A);
end
if any(A(:)<0)
    warning('MATLAB:centerOfMass:neg','Array A contains negative values.');
end

sz = size(A);
nd = ndims(A);
M = sum(A(:));
C = zeros(1,nd);
if M==0
    C = [];
else
    for ii = 1:nd
        shp = ones(1,nd);
        shp(ii) = sz(ii);
        rep = sz;
        rep(ii) = 1;
        ind = repmat(reshape(1:sz(ii),shp),rep);
        C(ii) = sum(ind(:).*A(:))./M;
    end
end

varargout = {C};

end
```

Compose image

```
function [ly, lx, Cx, Cy, image_phase, image_composed, w, image_composed_window] = gpa_compose_image(image
```

```
[ly, lx]=size(image);
if mod(lx,2)==1
    Cx=ceil(0.5*lx);

else
    Cx=ceil(0.5*lx)+1;
end

if mod(ly,2)==1
    Cy=ceil(0.5*ly);
else
    Cy=ceil(0.5*ly)+1;
end

image_composed = ones(size(image));
image_phase = image.*exp(1i*image_composed);
w = window2(ly,lx,@hann);
image_composed_window = image.*w;

end
```

Compose image

```
function [path_saved_images,folder_name] = gpa_create_folder(image_name,path_folder)  % var1 = image na

time = datestr(now,'dd-mm-yyyy--HH:MM');
filename = image_name;
A1 = time;
folder_name = sprintf('%s-%s',filename,A1);
mkdir (folder_name);
path_saved_images = [(path_folder),(folder_name)];

end
```

Displacement projection

```
function [alpha1, im_unwrapped_substracted_x1, im_unwrapped_substracted_y2] = gpa_displacement_projecti
```

```
angley = cursorpositiony-Cy;
anglex = cursorpositionx-Cx;
alpha1 = atan2(angley,anglex);
im_unwrapped_substracted_x1 = im_unwrapped_substracted * cosd(alpha1);
im_unwrapped_substracted_y2 = im_unwrapped_substracted * sind(alpha1);

end
```

FFT

```
function [Ftransform, Ftrasnfomr_shift, Ftransform_real_part, Ftransform_angle, Ftransform_real_part_shift

Ftransform = fft2(var);
Ftrasnfomr_shift = fftshift(Ftransform);

Ftransform_real_part = abs(Ftransform);
Ftransform_angle = angle(Ftransform);

Ftransform_real_part_shift = abs(Ftrasnfomr_shift);
Ftransform_angle_shift = angle(Ftrasnfomr_shift);

Ftransform_real_part_shift_log = log10(abs(Ftransform_real_part_shift));



end
```

Gaussian filter

```
function [moved_mask] = gpa_gaussian_filter (lx,ly,Cx,Cy,mass_centered_bragg_peak)

prompt = '3) What is the radius of the gaussian filter? Good idea to use the same one as in the circular m
R = input(prompt) % filter size parameter
X=0:lx-1; % x coordinates
Y=0:ly-1; % y coordinates
[X, Y] = meshgrid(X,Y);
gaussian_mask = exp(-((X-Cx).^2+(Y-Cy).^2)./(2*R).^2); % Centered in [1024,1024]

moved_mask=circshift(gaussian_mask,[Cy+round(mass_centered_bragg_peak(1))-3 Cx+round(mass_centered_bragg_p
```

```
end
```

GPA initialize

```
function [file_name_format,path_folder,image,path_image,image_name,format] = gpa_initialize ()

[file_name_format,path_folder] = uigetfile;
path_image = [(path_folder),(file_name_format)];
image = imread(file_name_format);
image = double(image);
image = image(:,:,1);
[unused,image_name,format] = fileparts(path_image);

end
```

Inverse FFT

```
function [a,iFimage_amp_fil,iFimage_ph_fil] = gpa_inverse_fft(Fimage_complex_sh,moved_mask)

Fimage_complex_sh_fil = Fimage_complex_sh.*moved_mask;
Fimage_amp_sh_fil = abs(Fimage_complex_sh_fil);
Fimage_ph_sh_fil = angle(Fimage_complex_sh_fil);
a = log10(Fimage_amp_sh_fil+1);

Fimage_complex_fil = fftshift(Fimage_complex_sh_fil);
iFimage_complex_fil = ifft2(Fimage_complex_fil);
iFimage_amp_fil = real(iFimage_complex_fil);
iFimage_ph_fil = angle(iFimage_complex_fil);

end
```

Plot color

```
function [name_figure] = gpa_plot_color(variable,fig_number,image_name,fig_title) %var1 is variable to be

figure(fig_number);
name_figure = imagesc(variable);
daspect([1,1,1]);
a = sprintf('%s %s',image_name, fig_title);
title(a);
set(0,'DefaultFigureWindowStyle','docked')
colorbar



end
```

Plot GPA

```
function [name_figure] = gpa_plot_gpa(variable,fig_number,image_name,fig_title);

figure(fig_number);
name_figure = imagesc(medfilt2(variable,[3,3]));
daspect([1,1,1]);
cmap = imread('colormap_gpa.png');
cmapd = im2double(squeeze(cmap(10,:,:)));
colormap(cmapd);
colorbar

a = sprintf('%s %s',image_name, fig_title);
title(a);
set(0,'DefaultFigureWindowStyle','docked')
set(gca,'YDir','normal')



end
```

Main code

Plot gray

```
function [name_figure] = gpa_plot_gray(variable,fig_number,image_name,fig_title) %var1 is variable to b

figure(fig_number);
name_figure = imagesc(variable);
daspect([1,1,1]);
colormap('gray');
a = sprintf('%s %s',image_name, fig_title);
title(a);
set(0,'DefaultFigureWindowStyle','docked')



end
```

Read Bragg peak coodinates

```
function [Fimage_amp_sh_log, cursorpositionx, cursorpositiony] = gpa_read_braggpeak_coordinates(var)

disp('1) Select the Bragg peak direction where you want to project the displacement. Click on the posit

figure(2)
Fimage_amp_sh_log=log10(var);
imagesc(Fimage_amp_sh_log)
title 'FFT power spectrum'
daspect([1,1,1]);
set(gca,'YDir','normal')
caxis('auto')
colormap('gray')

set(gcf,'CurrentCharacter',char(1));
h=datacursormode;
set(h,'DisplayStyle','datatip');
waitfor(gcf,'CurrentCharacter' ,char(32));
s = getCursorInfo(h);
pos = s.Position;
cursorpositionx = pos(1);
cursorpositiony = pos(2);
```

```
end
```

Strain reference

```
function [p1,p2,p3,zero_strain_region] = gpa_reference(zero_strain_region)

disp('4) Draw a rectangle to define a region of 0 strain (usually substrate). The bigger the region the be
figure(1)
zero_strain_region = imrect;
coordinates_zero_strain_region = getPosition(zero_strain_region);
coordinates_zero_strain_region_x_min = coordinates_zero_strain_region(1);
coordinates_zero_strain_region_y_min = coordinates_zero_strain_region(2);
coordinates_zero_strain_region_width = coordinates_zero_strain_region(3);
coordinates_zero_strain_region_height = coordinates_zero_strain_region(4);

p1 = [coordinates_zero_strain_region_x_min, coordinates_zero_strain_region_y_min];
p2 = [coordinates_zero_strain_region_x_min+coordinates_zero_strain_region_width, coordinates_zero_strain_r
p3 = [coordinates_zero_strain_region_x_min, coordinates_zero_strain_region_y_min+coordinates_zero_strain_r

end
```

Save image

```
function [full_name_path] = gpa_save_image(data,format,path,name)

full_name = [(name),(format)];
full_name_correct = [(path),('/')];
full_name_path = [(full_name_correct),(full_name)];

saveas(data,full_name_path);

end
```

GPA subtraction

```
function [phase_mean] = gpa_substraction (g,lx,ly)

x = 1:lx;
y = 1:ly;
[xm, ym] = meshgrid (x,y);
r = cat(3, ym,xm);
r2d = reshape(r,[lx*ly,2]);
phase_mean = 2*pi*g*r2d';
phase_mean = reshape(phase_mean,[ly,lx]);



end
```

Plane substraction

```
function [normal,plane,im_unwrapped_substracted] = gpa_substraction_plane(iFimage_ph_fil_unwr,p1,p2,p3)

p1 = round(p1);
p2 = round(p2);
p3 = round(p3);
p1(3) = iFimage_ph_fil_unwr(p1(2),p1(1));
p2(3) = iFimage_ph_fil_unwr(p2(2),p2(1));
p3(3) = iFimage_ph_fil_unwr(p3(2),p3(1));
normal = cross(p1 - p2, p1 - p3);
d = p1(1)*normal(1) + p1(2)*normal(2) + p1(3)*normal(3);
d = -d;
[ly, lx] = size(iFimage_ph_fil_unwr);
X=0:lx-1;
Y=0:ly-1;
[X,Y] = meshgrid(X,Y);
plane = (-d - (normal(1)*X) - (normal(2)*Y))/normal(3);
im_unwrapped_substracted = iFimage_ph_fil_unwr-plane;

end
```

Zero strain reference

```
cfunction [substraction_plane] = gpa_zero_strain_reference(zero_strain_region,iFimage_ph_fil_unwr,Lx,Ly)

p1 = [coordinates_zero_strain_region_x_min, coordinates_zero_strain_region_y_min];
p2 = [coordinates_zero_strain_region_x_min+coordinates_zero_strain_region_width, coordinates_zero_strain_r
p3 = [coordinates_zero_strain_region_x_min, coordinates_zero_strain_region_y_min+coordinates_zero_strain_r

p1(3)=iFimage_ph_fil_unwr(p1(2),p1(1));
p2(3)=iFimage_ph_fil_unwr(p2(2),p2(1));
p3(3)=iFimage_ph_fil_unwr(p3(2),p3(1));
normal = cross(p1 - p2, p1 - p3);
d = p1(1)*normal(1) + p1(2)*normal(2) + p1(3)*normal(3);
d = -d;
[Ly, Lx]=size(iFimage_ph_fil_unwr);
X=0:Lx-1;
Y=0:Ly-1;
[X,Y] = meshgrid(X,Y);
Z = (-d - (normal(1)*X) - (normal(2)*Y))/normal(3);
figure(13); mesh(X,Y,Z)

end
```

Window mask

```
function w=gpa_window2(N,M,w_func)

wc=window(w_func,N);
wr=window(w_func,M);
[maskr,maskc]=meshgrid(wr,wc);

w=maskr.*maskc;

end
```

6.5 Thickness fringes

Thickness fringes appear when crystal orientation perfectly match the Bragg condition. In this case the electrons will suffer constructive or destructive interference depending on the thickness of the material. Fig. 6.4 is an example of thickness fridges on the sides of a InSb NW. Since all TEM images are 2D projetions this is a good way to determine thickness variation in crystals.

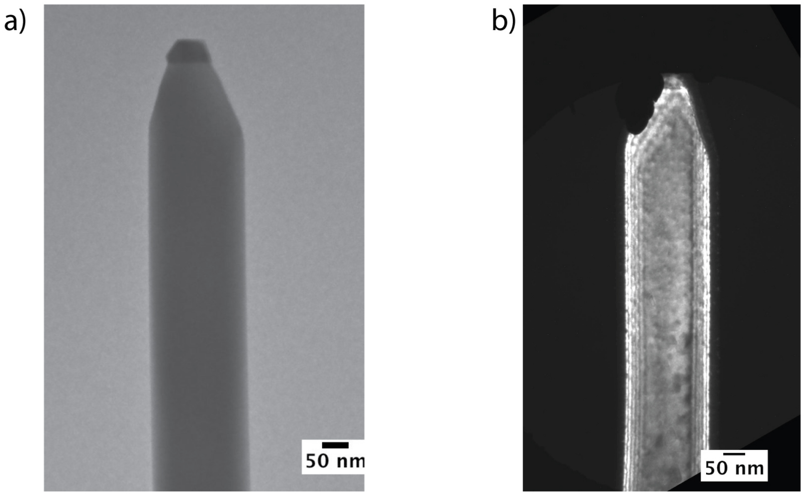

Figure 6.4: **a**) BF TEM image of an InSb NW.**b**) DF TEM image from a).

Bibliography

[1] I. Present, "Cramming more components onto integrated circuits," *Readings in computer architecture*, vol. 56, 2000.

[2] P. A. Packan, "Pushing the limits," *Science*, vol. 285, no. 5436, pp. 2079–2081, 1999.

[3] P. W. Shor, "Algorithms for quantum computation: Discrete logarithms and factoring," in *Foundations of Computer Science, 1994 Proceedings., 35th Annual Symposium on*, pp. 124–134, Ieee, 1994.

[4] J. Smith and M. Mosca, "Algorithms for quantum computers," *Handbook of Natural Computing*, pp. 1451–1492, 2012.

[5] L. K. Grover, "A fast quantum mechanical algorithm for database search," in *Proceedings of the twenty-eighth annual ACM symposium on Theory of computing*, pp. 212–219, ACM, 1996.

[6] D. P. DiVincenzo, "The physical implementation of quantum computation," *Fortschritte der Physik: Progress of Physics*, vol. 48, no. 9-11, pp. 771–783, 2000.

[7] B. E. Kane, "A silicon-based nuclear spin quantum computer," *nature*, vol. 393, no. 6681, p. 133, 1998.

[8] F. Kuemmeth, S. Ilani, D. Ralph, and P. McEuen, "Coupling of spin and orbital motion of electrons in carbon nanotubes," *Nature*, vol. 452, no. 7186, p. 448, 2008.

[9] R. Blatt and D. Wineland, “Entangled states of trapped atomic ions,” *Nature*, vol. 453, no. 7198, p. 1008, 2008.

[10] J. P. Home, D. Hanneke, J. D. Jost, J. M. Amini, D. Leibfried, and D. J. Wineland, “Complete methods set for scalable ion trap quantum information processing,” *Science*, vol. 325, no. 5945, pp. 1227–1230, 2009.

[11] J. Majer, J. Chow, J. Gambetta, J. Koch, B. Johnson, J. Schreier, L. Frunzio, D. Schuster, A. Houck, A. Wallraff, *et al.*, “Coupling superconducting qubits via a cavity bus,” *Nature*, vol. 449, no. 7161, p. 443, 2007.

[12] A. J. Keller, P. B. Dieterle, M. Fang, B. Berger, J. M. Fink, and O. Painter, “Superconducting qubits on silicon substrates for quantum device integration,” *arXiv preprint arXiv:1703.10195*, 2017.

[13] J. Sherson, A. S. SÃÿrensen, J. FiurÃąÅąek, K. MÃÿlmer, and E. S. Polzik, “Light qubit storage and retrieval using macroscopic atomic ensembles,” *Physical Review A*, vol. 74, no. 1, pp. 011802–+, 2006.

[14] S. Gazibegovic, D. Car, H. Zhang, S. C. Balk, J. A. Logan, M. W. de Moor, M. C. Cassidy, R. Schmits, D. Xu, G. Wang, *et al.*, “Epitaxy of advanced nanowire quantum devices,” *Nature*, vol. 548, no. 7668, p. 434, 2017.

[15] Y. Oreg, G. Refael, and F. von Oppen, “Helical liquids and majorana bound states in quantum wires,” *Physical review letters*, vol. 105, no. 17, p. 177002, 2010.

[16] A. Y. Kitaev, “Fault-tolerant quantum computation by anyons,” *Annals of Physics*, vol. 303, no. 1, pp. 2–30, 2003.

[17] B. Field and T. Simula, “Introduction to topological quantum computation with non-abelian anyons,” *Quantum Science and Technology*, 2018.

[18] Q. L. He, L. Pan, A. L. Stern, E. C. Burks, X. Che, G. Yin, J. Wang, B. Lian, Q. Zhou, E. S. Choi, *et al.*, “Chiral majorana fermion modes in a quantum anomalous hall insulator–superconductor structure,” *Science*, vol. 357, no. 6348, pp. 294–299, 2017.

[19] R. M. Lutchyn, J. D. Sau, and S. D. Sarma, "Majorana fermions and a topological phase transition in semiconductor-superconductor heterostructures," *Physical review letters*, vol. 105, no. 7, p. 077001, 2010.

[20] W. Chang, S. Albrecht, T. Jespersen, F. Kuemmeth, P. Krogstrup, J. Nygård, and C. M. Marcus, "Hard gap in epitaxial semiconductor–superconductor nanowires," *Nature nanotechnology*, vol. 10, no. 3, p. 232, 2015.

[21] M. Barkeshli and J. D. Sau, "Physical architecture for a universal topological quantum computer based on a network of majorana nanowires," *arXiv preprint arXiv:1509.07135*, 2015.

[22] O. GuÌĹl, H. Zhang, F. K. de Vries, J. van Veen, K. Zuo, V. Mourik, S. Conesa-Boj, M. P. Nowak, D. J. Van Woerkom, M. Quintero-PeÌĄrez, *et al.*, "Hard superconducting gap in insb nanowires," *Nano letters*, vol. 17, no. 4, pp. 2690–2696, 2017.

[23] S. M. Sze and K. K. Ng, *Physics of semiconductor devices.* John wiley & sons, 2006.

[24] R. Wagner and W. Ellis, "Vapor-liquid-solid mechanism of single crystal growth," *Applied Physics Letters*, vol. 4, no. 5, pp. 89–90, 1964.

[25] P. Krogstrup, N. Ziino, W. Chang, S. Albrecht, M. Madsen, E. Johnson, J. Nygård, C. Marcus, and T. Jespersen, "Epitaxy of semiconductor–superconductor nanowires," *Nature materials*, vol. 14, no. 4, p. 400, 2015.

[26] S. Yokoyama, J. Oogi, D. Yui, and M. Kawabe, "Low-temperature selective growth of gaas by alternately supplying molecular beam epitaxy," *Journal of Crystal Growth*, vol. 95, no. 1-4, pp. 32–34, 1989.

[27] L. Desplanque, M. Fahed, X. Han, V. Chinni, D. Troadec, M. Chauvat, P. Ruterana, and X. Wallart, "Influence of nanoscale faceting on the tunneling properties of near broken gap inas/algasb heterojunctions grown by selective area epitaxy," *Nanotechnology*, vol. 25, no. 46, p. 465302, 2014.

[28] F. Krizek, J. E. Sestoft, P. Aseev, S. Marti-Sanchez, S. Vaitiekenas, L. Casparis, S. A. Khan, Y. Liu, T. Stankevic, A. M. Whiticar, *et al.*, "Field effect enhancement in buffered quantum nanowire networks," *arXiv preprint arXiv:1802.07808*, 2018.

[29] J. R. Arthur Jr, "Technique for growth of epitaxial compound semiconductor films," Oct. 26 1971. US Patent 3,615,931.

[30] J. Orton and T. Foxon, *Molecular beam epitaxy: a short history.* Oxford University Press, USA, 2015.

[31] M. Henini, *Molecular beam epitaxy: from research to mass production.* Newnes, 2012.

[32] J. Haeni, C. Theis, and D. Schlom, "Rheed intensity oscillations for the stoichiometric growth of srtio 3 thin films by reactive molecular beam epitaxy," *Journal of Electroceramics*, vol. 4, no. 2-3, pp. 385–391, 2000.

[33] U. M. Bhatta, J. Dash, A. Roy, A. Rath, and P. Satyam, "Formation of aligned nanosilicide structures in a mbe-grown au/si (110) system: a real-time temperature-dependent tem study," *Journal of Physics: Condensed Matter*, vol. 21, no. 20, p. 205403, 2009.

[34] M. Friedl, K. Cerveny, P. Weigele, G. TuÌĹtuÌĹncuÌĹoglu, S. Martí-Sánchez, C. Huang, T. Patlatiuk, H. Potts, Z. Sun, M. O. Hill, *et al.*, "Template-assisted scalable nanowire networks," *Nano letters*, vol. 18, no. 4, pp. 2666–2671, 2018.

[35] D. Alexander, "Cm 20 user guide." Available online at *https : //cime.epfl.ch/Files/Teaching/TEM20user20manuals/CM2020user20guide.pdf*.

[36] D. T. U. Wind Energy Department, "Jeol jem 3100f." Available online at *https : //www.jeol.co.jp/en/products/detail/JEM − 3100F.html*.

[37] L. de Microscopia Avanzada, "Fei titan 3 c's corrected specifications." Available online at *http : //ina.unizar.es/research/laboratories/uhrtem − laboratory/*.

[38] D. Spirkoska, J. Arbiol, A. Gustafsson, S. Conesa-Boj, F. Glas, I. Zardo, M. Heigoldt, M. Gass, A. L. Bleloch, S. Estrade, *et al.*, “Structural and optical properties of high quality zinc-blende/wurtzite gaas nanowire heterostructures,” *Physical Review B*, vol. 80, no. 24, p. 245325, 2009.

[39] M. Hÿtch, E. Snoeck, and R. Kilaas, “Quantitative measurement of displacement and strain fields from hrem micrographs,” *Ultramicroscopy*, vol. 74, no. 3, pp. 131–146, 1998.

[40] S. Nakamura, M. Senoh, N. Iwasa, and S.-i. Nagahama, “High-brightness ingan blue, green and yellow light-emitting diodes with quantum well structures,” *Japanese journal of applied physics*, vol. 34, no. 7A, p. L797, 1995.

[41] S. K. Patra and S. Schulz, “Electrostatic built-in fields in wurtzite iii-n nanostructures: Impact of growth plane on second-order piezoelectricity,” *Physical Review B*, vol. 96, no. 15, p. 155307, 2017.

[42] M. Hÿtch and T. Plamann, “Imaging conditions for reliable measurement of displacement and strain in high-resolution electron microscopy,” *Ultramicroscopy*, vol. 87, no. 4, pp. 199–212, 2001.

[43] F. Hüe, M. Hÿtch, H. Bender, F. Houdellier, and A. Claverie, “Direct mapping of strain in a strained silicon transistor by high-resolution electron microscopy,” *Physical review letters*, vol. 100, no. 15, p. 156602, 2008.

[44] B. Goris, J. De Beenhouwer, A. De Backer, D. Zanaga, K. J. Batenburg, A. SaÌĄnchez-Iglesias, L. M. Liz-MarzaÌĄn, S. Van Aert, S. Bals, J. Sijbers, *et al.*, “Measuring lattice strain in three dimensions through electron microscopy,” *Nano letters*, vol. 15, no. 10, pp. 6996–7001, 2015.

[45] A. Deal, T. Hooghan, and A. Eades, “Energy-filtered electron backscatter diffraction,” *Ultramicroscopy*, vol. 108, no. 2, pp. 116–125, 2008.

[46] M. Borland, “A high brightness thermionic microwave electron gun,” tech. rep., 1991.

[47] W. Coene, G. Janssen, M. O. de Beeck, and D. Van Dyck, "Phase retrieval through focus variation for ultra-resolution in field-emission transmission electron microscopy," *Physical Review Letters*, vol. 69, no. 26, p. 3743, 1992.

[48] australian Microscopy and M. Society, "Lens and apertures." Available online at $http://www.ammrf.org.au/myscope/tem/introduction/$.

[49] C. Hetherington, "Aberration correction for tem," *Materials Today*, vol. 7, no. 12, pp. 50–55, 2004.

[50] A. Bleloch and A. Lupini, "Imaging at the picoscale," *Materials Today*, vol. 7, no. 12, pp. 42–48, 2004.

[51] J. Venables, G. Spiller, and M. Hanbucken, "Nucleation and growth of thin films," *Reports on Progress in Physics*, vol. 47, no. 4, p. 399, 1984.

[52] J. T. M. De Hosson and V. Vitek, "Atomic structure of (111) twist grain boundaries in fcc metals," *Philosophical Magazine A*, vol. 61, no. 2, pp. 305–327, 1990.

[53] C. Thompson, J. Floro, and H. I. Smith, "Epitaxial grain growth in thin metal films," *Journal of applied physics*, vol. 67, no. 9, pp. 4099–4104, 1990.

[54] I. Ponomareva, M. Menon, D. Srivastava, and A. N. Andriotis, "Structure, stability, and quantum conductivity of small diameter silicon nanowires," *Physical review letters*, vol. 95, no. 26, p. 265502, 2005.